UNIVERSITÀ DEL SALENTO

FACOLTÀ DI SCIENZE MATEMATICHE FISICHE E NATURALI

PhD THESIS

METAL-LESS GRAPHITIC CONTACTS ON CVD DIAMOND FOR NUCLEAR DETECTOR APPLICATIONS

Committee:	PhD Student:
Ch.mo Prof. MAURIZIO MARTINO	EMANUELE ALEMANNO
Ch.mo Dr. GABRIELE CHIODINI	

JULY 2013

Contents

Introduction

Due to its exceptional electrical, thermal and optical properties, Chemical Vapor Deposition (CVD) diamond is a very attractive material for radiation detection. Diamond can detect any kind of radiation that is more energetic than its bandgap of 5.47 eV, e.g., deep UV photons, X-rays, gamma rays, charged particles and neutrons with energies ranging from 5.47 eV up to GeV of cosmic rays. Because of its radiation hardness it needs no frequent replacements, it can work at room temperature with no need for cooling, it has a resistivity several orders of magnitude greater than silicon, it has an extremely low leakage current and no need for p-type or n-type junctions as required in silicon radiation detectors. Diamond radiation detectors are generally designed as a solid state ionization chamber mainly in two configurations: with electrodes up and down the plate (called "Sandwich" configuration) or interdigitated electrodes on a surface. A charged particle passing through diamond releases in average 13 eV to produce an electron-hole pair ([1]). The produced pairs are separated in presence of an electric field. Electrons drift towards the positive electrode, while holes drift in the opposite direction. As the free carriers move, a charge is induced on the electrodes, which can be integrated by a charge-sensitive preamplifier [2].

The aim of this thesis work is to make Ohmic graphite electrical contacts on diamond surface to create different types of diamond detectors for high energy nuclear applications. For this reason we proved the capability of diamond to give a response before and after damage by heavy irradiation. In order to create graphite layers we focused a pulsed excimer laser on a polycrystalline thermal grade CVD diamond surface operating at KrF (wavelength 248 nm) and ArF (wavelength 193 nm). To investigate the structure and the morphology of the generated pads for each laser wavelength we performed micro-Raman and photo-luminescence (PL) measurements along with Scanning Electron Microscopy (SEM). The results obtained on previous diamond type were used to graphitise a polycrystalline detector grade CVD diamond to make a device with graphite electrical contacts fabricated on both faces of the diamond surfaces. The device was prepared by front and back irradiation of the diamond bulk by a 193 nm ArF excimer laser. In order to prove the Ohmic behaviour of the electrodes, leakage dark current measurements were carried out and to realize that diamond is capable to detect nuclear radiation in counting mode we evaluated the responses of the device under accelerated proton beams and γ-rays. While in order to verify the response of the device after and before radiation damage by a 62 MeV proton beam with an integrated fluence of $(2.00\pm0.08)\times10^{15}$ protons/cm^2 for 1.5 exposure days, we stimulated diamond detector by β-rays and proton beams.

The next step was to make a new type of device, the strip device, made by 20 graphite strips in front of diamond surface and a uniform graphite pad in the back. The strips had a width of about 100 μm, a length of 3.5 mm and a spacing between electrodes of 68 μm. In order to have preliminary results about this new device we performed resistance measurements on graphite electrodes and between two different electrodes to have the surface resistivity of diamond. In addition, we measured the leakage current between a fixed strip and the uniform graphite pad on the other side of the sample.

Finally, we concluded with the making of a three strips detector. The aim of three strips detector is to compare the efficiency of charge collection among three electrodes with the same geometry, but created on diamond surface with different techniques. A first characterization was made by investing the device with a beam of β-rays in order to evaluate the response of the three strips.

Chapter 1

CVD Diamond: general properties and synthesis

The Greek word "$\alpha\delta\acute{\alpha}\mu\alpha\varsigma$", meaning unconquerable and indestructible, is the root word of diamond. By every measure, diamond is a unique material. Its supreme hardness, singular strength, high thermal conductivity, chemical inertness, excellent optical properties as well as extraordinary semiconductor behaviour of the material attracts scientific and technological interest worldwide ever since decades. However, only the recently developed Chemical Vapor Deposition (CVD) technique and in particular the homoepitaxial growth allowed reproducible synthesis of high quality CVD diamond. Thus CVD diamond can be referred to as a novel material.

1.1 Intrinsic properties of CVD diamond

Diamond is composed of carbon atoms arranged in the tetrahedron diamond lattice (Fig.1.1). The atoms stick together through strong sp^3 σ-type bonds. The small carbon atoms give a very dense, but low weight lattice. These facts give reason for the extraordinary characteristics of diamond. It consists of two interpenetrating face-centered cubic lattices, displaced along the diagonal of the cubic cell by one quarter of length of the diagonal. It can also be regarded as a face-centered cubic lattice with a basis of two carbon atoms at $\mathbf{0}$ and $(a/4)(\hat{\mathbf{x}}+\hat{\mathbf{y}}+\hat{\mathbf{z}})$, where a is the lattice constant, which is equal to 3.57 $\mathring{A}$ for diamond, 5.43 $\mathring{A}$ and 5.66 $\mathring{A}$, respectively, for Si and Ge which crystallize in the same structure. Diamond exhibits a series of extreme physical properties.

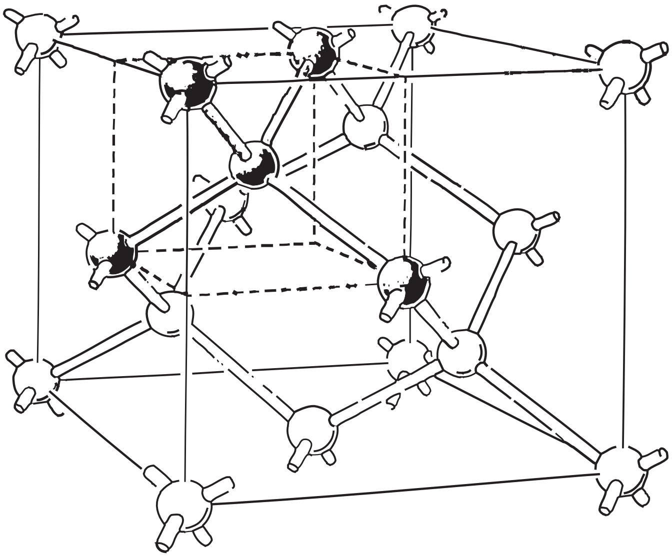

Fig. 1.1. The unit cell of diamond [3].

It has the highest atom number density of any terrestrial material, 1.76×10^{23} atoms/cm^3. It is the hardest of all solids and has the highest elastic moduli. As a consequence, it has the highest sound velocity and the lowest compressibility. It has the highest room temperature thermal conductivity, 20 W/cm K (four times that of copper). Its coefficient of thermal expansion, 0.8×10^{-6} K^{-1} is less than that of Invar at 293 K. Diamond has an electronic structure similar to silicon and germanium, since all three crystals have four valence bands and an indirect bandgap [4]. The larger bandgap of diamond, 5.5 eV, is related to its stronger bond. As a consequence of this large bandgap, pure diamond is an excellent electrical insulator (the resistivity can be as high as 10^{16} Ω·cm), and exhibits no absorption of optical radiation for energies below about 5.5 eV, that corresponds to a wavelength of 225 nm, well into the far UV spectral region. Absorption in the one-phonon region is forbidden, since, because of the cubic symmetry, the phonon modes of lattice are infrared inactive. However, diamond exhibits two intrinsic absorption bands, located between about 4000 and 1500 cm^{-1}, corresponding to the two-phonon (3.75-7.51 μm) and the three-phonon (2.50-3.75 μm) absorption bands, which are

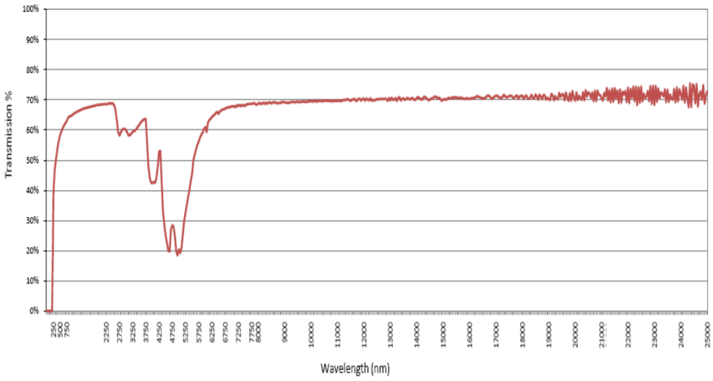

Fig. 1.2. UV/Visible/NIR and FT-IR transmission spectrum for polycristalline CVD diamond optical grade given to us by Diamond Detectors Ltd company.

bonded by multiples of the Raman frequency (1332 cm^{-1}) [5, 6], i.e. the maximum vibrational frequency of the lattice. Since diamond is an indirect bandgap semiconductor, band-to-band electronic absorption can only occur with the participation of phonons.

Fig.1.2 shows the trasmission spectrum of a polycristalline CVD diamond optical grade in the UV/Visible/NIR and FT-IR regions given to us by Diamond Detectors Ltd company. We can see that diamond trasmittance approaches its theoretical maximum of 70%, limited by reflection. Therefore, an ideal perfect diamond, free from impurities and defects, presents no absorption in the visible region from 0.4 to 0.7 μm and is therefore completely colourless.

1.2 Synthesis of CVD diamond film

In this section we review the most important topics on diamond film synthesis. The general conditions for diamond growth will be discussed, a brief overview of the different CVD methods will be given, aimed to point out the main achievements and the problems still unresolved.

1.2.1 Historical Background

One of the most important developments in diamond synthesis is Chemical Vapor Deposition (CVD). The first attempt at creating diamond using a CVD process was reported by Eversole in 1949 [7]. A milestone in the diamond CVD technique was the discovery by Soviet researchers of the role of atomic hydrogen in removing unwanted graphitic phase but leaving diamond unaffected [8, 9]. Although the Soviet successes were largely ignored in the U.S.A., this discovery launched a significant period of exploration of various CVD techniques for synthesizing diamond films and coatings in the 1980s in the Soviet Union and Japan [10, 11]. In 1982, a group at the National Institute for Research in Inorganic Materials (NIRIM), Japan, had built a first reactor dedicated for diamond growth and reported growth rates for diamond films of up to 10 μm/h [12]. Also at NIRIM, the first investigation of homoepitaxial diamond films using the microwave plasma enhanced CVD (MWPECVD) method was undertaken by Kamo et al. [13], following his demonstration of MWPECVD for polycrystalline diamond growth [11]. The first high quality electronic grade scCVD diamonds of extraordinary carrier mobilities and lifetimes were grown by Element Six in 2002 [14]. Although nowadays electronic grade scCVD diamond is commercially available it is still considered as an R&D (Research and Development) material.

1.2.2 Basics of the CVD tecnique

As its name implies, chemical vapor deposition involves a gas phase chemical reaction occurring above a solid surface, which causes deposition onto that surface. All CVD techniques for producing diamond films require a means of activating gas phase containing carbon precursor molecules. The activation can involve thermal methods (e.g., a hot filament), electric discharge (e.g., DC, RF or microwave), or a combustion flame (such as an oxyacetylene torch). While each method differs in detail, they all share a few features in common: the precursor gas (usually CH_4) is diluted in excess of hydrogen, in a typical mixing ratio of 1-15% vol. CH_4. Also, the temperature of the substrate is usually greater than 700 °C to ensure the formation of diamond rather than amorphous carbon. The schematics in Fig.1.3 show the basics of CVD chemistry. The process gases first mix in the chamber before diffusing toward the substrate surface. En route, they pass through an activation region (e.g. electric discharge), which causes molecules to fragment into

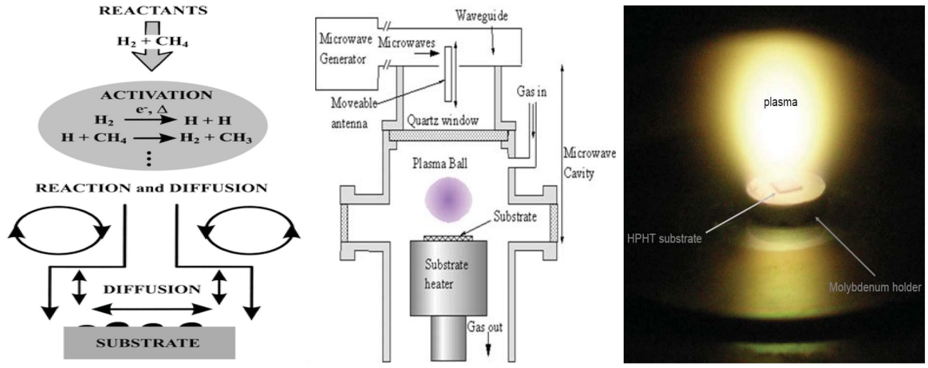

Fig. 1.3. (Left panel) A schematic illustrating some of the more important physico-chemical processes occurring during diamond CVD using a CH_4/H_2 input gas mixture [15]. (Middle panel) A schematic of the most popular ASTEX-type research reactor for microwave plasma enhanced chemical vapour deposition (MWPECVD) diamond growth. (Right panel) A photograph of scCVD diamond growth process in a MWPECVD ASTEX-type reactor (courtesy N. Tranchant [16]).

reactive radicals and atoms and heats the gas up to temperatures approaching a few thousand Kelvins. When species reach the substrate a surface reaction occurs, where one of possible outcome, if all the conditions are suitable, is diamond. Atomic hydrogen plays an essential role in the surface and plasma chemistry of diamond deposition. Two effects are believed crucial to the growth of CVD diamond:

- The bulk of diamond is fully sp^3 bonded. However at the surface there is effectively a dangling bond, which needs to be terminated in order to prevent reconstruction of the surface to graphite. This surface termination is performed by hydrogen, which keeps the sp^3 diamond lattice stable.

- Atomic H is known to etch graphitic sp^2 carbon many times faster than diamond-like sp^3 carbon.

Additionally in the chemistry of the plasma:

- H atoms are efficient scavengers of long-chained hydrocarbons, breaking them up into smaller pieces. This prevents the build-up of polymers in the gas phase, which might deposit onto the substrate and inhibit diamond growth.

- H atoms react with neutral species such as CH_4 to create reactive radicals, such as CH_3, which can then attach to suitable surface sites.

A detailed review of the various methods used for fabricating diamond can be found in [17].

1.2.3 Outline of the mechanism of CVD diamond growth

The three basic stages of the CVD process are:

1. Formation of atomic hydrogen.
2. Process of nucleation.
3. Growth of diamond.

Formation of atomic hydrogen

In CVD systems molecular hydrogen is dissociated into atomic hydrogen by various methods as explained in section 1.2.2 about the activating techniques for gas phase containing carbon precursor molecules. The overabundance of atomic hydrogen with respect to the equilibrium concentration has a predominant role in diamond growth. Atomic hydrogen plays mainly three functions:

1. reacts with graphite 20 ÷ 30 times faster than the diamond up to substrate temperature < 1300 °C [18]; in this way the graphite and other phases different from sp^3 diamond are removed rapidly from the substrate and it prevents the incorporation of graphite into diamond growth; this is the gasification of graphite by the atomic hydrogen to form methane, which involves a large negative free-energy change:

$$C_g + 4H(g) \rightarrow CH_4(g) \tag{1.1}$$

2. transforms hydrocarbons into radicals, which are the precursors necessary for the growth of diamond, for example:

$$CH_4 + H(g) \rightarrow CH_3^{\cdot} + H_2(g) \tag{1.2}$$

3. extracts hydrogen from hydrocarbons linked to the growth surface, leaving a site active that allows the absorption of another hydrocarbon to be part of the surface:

   $$\mathrm{C}_d\mathrm{H} + \mathrm{H}\ (\mathrm{g}) \rightarrow \mathrm{C}_d^* + \mathrm{H}_2\ (\mathrm{g}) \tag{1.3}$$

   where C_d refers to a carbon-bonded diamond and C_d^* is the same atom with a free bond.

Diamond nucleation

The formation of nuclei for diamond growth on the substrate is called nucleation; for **heteroepitaxial** diamond growth, i.e. for nondiamond substrates (Si [19], Mo [20], W [20], SiC [20], Cu [20], WC [21]) nucleation is distinct from the growth process, because it requires a different chemical composition of the plasma activated. For example in [22] diamond powders with grain diameters up to 0.3 μm were obtained by CO_2-laser-induced decomposition of C_2H_4 at low pressures and temperatures. C_2H_4 or mixtures of C_2H_4, H_2 and SiH_4 were irradiated in a gas-flow reactor by tunable CO_2 laser (10.532 μm). The product contained polyaromatic species, high molecular polymers, graphite, amorphous carbon and spherical diamond particles. Several diamond particle populations, with mean diameters of 6-120 nm, were observed by transmission electron microscopy [22]. Very probably diamond nucleation is thought to being with adsorption on the substrate of sp^2 bonded gaseous species such as polycyclic aromatic hydrocarbons (PAHs) [23]. (PAHs) are formed in the gas phase through hydrogen abstraction and other chemical reactions [24]. After adsorption on the substrate surface, these sp^2 bonded species can either desorb, be etched away by atomic hydrogen, or form stable nuclei [23]. Stability can be achieved through conversion of sp^2 bonds to sp^3 through hydrogen abstraction. The saturated carbon molecule which results from this process has a dramatically reduced surface energy relative to that of the original sp^2 bonded nucleus [23] and is therefore more stable. The layer of diamond is formed mainly through continuous growth of grains rather than through the additional nucleation on the surface of the substrate; to grow a layer of diamond cohesive and uniform, it is therefore necessary that the sites of nucleation are produced with sufficient density ($> 10^9$ nuclei/cm^{-2}) [25]. The process of nucleation necessary to obtain a sufficient density of nuclei of growth typically lasts few hours. It's important the increasing of nucleation velocity and the density to ensure a good quality of diamond and to

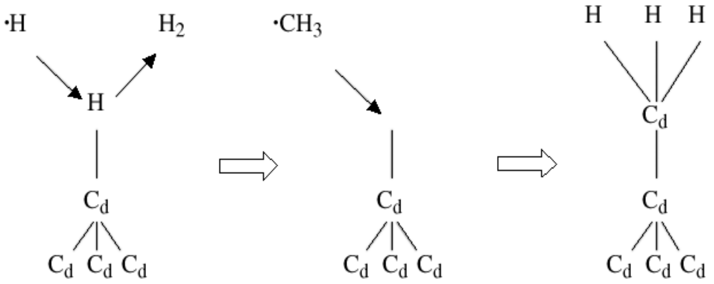

Fig. 1.4. A possible reaction schemes for the growth of CVD diamond film.

avoid the formation of carbon atoms in sp^2 state. For this reason they have been introduced new procedures for these purposes. For example in ref. [26] the nucleation and growth of diamond on two-step pretreated Si substrates were studied. The diamond films were produced by hot-filament chemical vapor deposition. The two-step pretreatment comprised coating the smooth Si substrate with a thin carbon film by electrolysis of methanol solution, followed by 1 min ultrasonic treatment with diamond powder. An enhanced diamond nucleation density as high as 2×10^9 cm^{-2} was obtained, three orders of magnitude higher than that on single-step pretreated Si substrates. In addition, rapid diamond nucleation on the pretreated Si substrate was observed. Explanation is given by the scratching of the surface by abrasion of diamond powder that plays an important role in the nucleation behaviour [27]. Other methods to increase the nucleation depend on chemical changes in the surface of the substrate: it is generally found a layer of polycrystalline carbide at the interface between the diamond and the substrate [28].

The most effective way to obtain a single crystal diamond is for **homoepitaxial** diamond growth, i.e. for diamond substrate [29]. In this case the nucleation is not different from the process of growth and any special precaution is therefore not required to control it. Unfortunately the use of a single crystal as substrate limits the size of the CVD diamond to that of starting diamond and therefore this technique is unsuitable for the manufacture on industrial scale.

Diamond growth

An understanding of diamond film growth under CVD conditions is attributed to the role of atomic hydrogen. Fig.1.4 shows the possible reaction process. Atomic hydrogen and methyl radicals, which come into being by thermal or electronic methods, are the important growth precursors for diamond. Generally, the dangling bonds of carbon atoms on the growing surfaces of diamond film were terminated by atomic hydrogen to prevent the surfaces from reconstructing to the graphite-like surface. Due to the stronger H-H bond in molecular hydrogen than the C-H bond, the surface-bonded atomic hydrogen can be abstracted by a gas phase atomic hydrogen with the formation of a stable molecular hydrogen and lead to activating a vacant site. This process is called the abstraction effect of atomic hydrogen. Then a methyl radical occupies this vacant site to form a new C-C bond, therefore providing a possible extension of the diamond lattice. In addition, atomic hydrogen can etch both diamond and graphite. These processes indicate that the abstraction of atomic hydrogen and the etching of atomic hydrogen to diamond and graphite on the diamond growth surface influence the growth, growth rate, and the quality of the diamond film [30].

Chapter 2

Radiation detectors based on synthetic diamond

The state of the art of Chemical Vapor Deposition (CVD) diamond detector technology is reviewed and its applications in several fields, such as high-energy physics, radiotherapy and nuclear fusion reactors, are described. The impact of the newest front-end electronics design is discussed.

2.1 Introduction

Particle detectors are usually composed of a sensitive volume and an amplification stage. The sensitive volume of high-quality solid-state sensor is usually characterized by a low intrinsic carrier density. In the case of narrow-band gap semiconductors e.g., silicon, pn-junction must be formed in order to obtain a sensitive volume with low carrier concentration. In the case of wide-band gap semiconductors like diamond, the sensitive volume is given only by the geometry of the electrodes. A charged particle impinging the sensitive volume, produces e-h pairs by the ionization process. After fast thermalization, order of a few ps, the carriers start to drift under the influence of an external applied electric field. The induced current or charge (q_{ind}) on the electrodes is read-out either directly using broadband electronics or it is integrated by charge sensitive electronics, giving a signal proportional to the deposited energy. The drift length of the excess carriers is limited by their lifetime and their velocity. If the lifetime is much longer than the drift time of the carriers within the sensitive volume, the total charge measured is equal to the number of primary created e-h pairs. In order to optimize the detector signal it is important to improve the carrier lifetime and thus the crystal quality at the best. Diamond quality is also strongly related to the charge collection distance $\lambda = \lambda_e + \lambda_h$, which is the distance e-h pair drift apart, due to the electric field E, before trapping or recombination occurs. For Minimum Ionizing Particles (MIP) in counting mode, the induced electric pulse is given by [31]: $q_{ind}=36\frac{e^-}{\mu m}\lambda[1 - \frac{\lambda}{d}(1 - e^{-\frac{d}{\lambda}})]$, where d is the distance between biasing electrodes.

Polycrystalline diamond is produced by Chemical Vapour Deposition (CVD) from energized H_2(98%)+CH_4(2%) gas mixtures. Diamond is a semiconductor with outstanding material properties such as high radiation hardness, high free carrier mobilities, very low leakage current, and very high thermal conductivity. High quality CVD diamond can be used as radiation detector which is in many ways much simpler than silicon radiation detectors. In fact, diamond is not doped; metallic electrodes are simply placed on device surface; the signal is collected by a charge sensitive amplifier; no leakage current compensation is needed; no cooling is required. Diamond detectors are successfully employed in several scientific and technical fields where the signal is not a concern but radiation tolerance and fast response are mandatory. These applications are mainly heavy ions detection (see GSI experiments at Darmstadt in Germany) and beam or X-ray monitoring (intense synchrotron light, FEL, and inertial fusion sources)[32]. Nevertheless, in the last years large size and free-standing polycrystalline diamond are produced with high quality and good reproducibility, making this material attractive for very demanding applications such as tracking detectors and bidimensional dosimeters for Intensity Modulated Radiation Therapy (IMRT).

2.2 Applications

Diamond detectors are sensitive to any kind of radiations: from deep UV light to X and γ rays, from α and β radiations to neutrons, so that a large variety of applications can be envisaged.

Single channel devices, readout by a quite traditional electronic chain, are used when position information is not required, such as in monitoring and dosimetry. Electrodes patterning in micro-strips and pixels by lithography are necessary in tracking and vertexing reconstruction, such as in high energy physics. In addition, advanced interconnection techniques between sensors and front-end electronics are required to realize multi-channel hybrid devices.

2.2.1 Detectors for tracking in high energy physics

Diamond hybrid pixel prototypes were assembled with standard ATLAS pixel electronics (FE- I3) using Ti-W metallization and IZM solder bump-bonding [33]. An entire ATLAS module, made of high quality polycrystal diamond and equipped with 16 front-end chips, showed more than 97% of working channels and a global threshold setting as low as 1500 e^-. In addition, single crystal diamond sensor was bump-bonded to single chip showing almost ideal performance. All these prototypes, after calibration in the laboratory with radioactive source, were fully characterized in high-energy particle beams before and after irradiation showing very good results in terms of efficiency and in-time spatial resolution.

2.2.2 Pixellated detectors for IMRT

Modern radiotherapy is based on IMRT, which delivers dose to a 3D target irradiating the patient through many photons beams in different directions, and entry points, in order to maximize the radiation field on the tumor and minimize it on healthy tissues. The LINAC accelerator is equipped with multi-leaf collimators and the radiation detection system is typically based on commercial single side silicon strip detectors.

The tissue equivalence, linearity over three dose decades, and radiation hardness make diamond a very attractive material for next generation of IMRT radiation detection system. For this applications the signal-to-noise ratio is not of a concern but linearity and stability of the response are crucial (about 0.5% precision). Very promising is polycrystal diamond in null-bias operation [34], where a Schottky barrier at the metal-diamond interfaces is created and an active region is established, due to the built-in electric field. In this condition the charge carriers do not cross the diamond bulk and the dynamic response is unaffected by trapping mechanism due to bulk defects.

2.2.3 Detectors for monitoring and nuclear spectroscopy

Polycrystalline diamond for beam condition monitoring (BCM) or beam loss monitoring (BLM) were pioneered by the BaBar, Belle, and CDF collaborations. All four experiments at LHC installed diamond beam monitoring, demonstrating that diamond is a mature material for this application [33].

Being diamond a low Z material it can be used for beta and alpha monitoring in presence of high gamma background. Thermal neutrons can be detected using converters, like ^{10}B or ^{6}Li, and fast neutrons using reactions on carbons ^{12}C. In both cases short range energetic ions are generated and large signals detected [35]. Spectroscopy-grade detector can be manufactured using single crystal diamond grown by homoepitaxy from a seed of special oriented HPHT (High Pressure High Temperature). This method limits the single crystal diamond size to the HPHT substrate size of $\sim 5\times5$ mm^2 [29].

2.3 Low noise and fast front-end for pixels

The negligible leakage current and the small detector capacitance result in a low intrinsic noise of the diamond detectors which might compensate the disadvantage of the small signal size if sufficiently low noise front-end electronics, operating at effective threshold below 1000 e$^-$, were available. Vertically integrated pixels may be the solution to many limitations of the traditional CMOS technology. In fact, multilayer device structure can keep analog and digital pixel-level electronics on different tiers, reducing substrate and power distribution cross-talks, increasing complexity and functionality, and reducing pixel size [36].

Presently, the electronic noise is the limiting factor of the excellent time resolution of CVD diamond detectors. Time resolution is given by the signal rise-time and signal-to-noise ratio according to the formula: $\sigma_T = T_{rise}/\frac{S}{N}$. Assuming T_{rise} =1 ns and $\frac{S}{N}$=20 the formula predicts a 50 ps time resolution for the ideal case. For a MIP signal this can be achieved only if the first stage amplifier is integrated on the detector and an adequate amplification-shaping stage follows [37]. For pixel detectors the power consumption is a strong limitation but pixel readout chip with excellent time resolution (better than 100 ps) are developed for the Gigatracker of NA62 experiment [38].

Chapter 3

Graphitization process on CVD diamond plate

In this chapter we talk about graphitization process on CVD diamond plate in order to create conductive graphitic layers on diamond surface that we'll use as conductive electrodes to make detectors for nuclear applications. Graphitization process can occur by pulsed (width pulse: 20 ns) excimer laser irradiation on diamond surface, i.e. by ArF (193 nm) [39] or by KrF (248 nm) [40]. This technique transfer energy to carbon atoms and they pass from diamond state to graphite state, because diamond is a metastable state for carbon that rearranges its electron shell and it can pass to graphite state. In order to evaluate the nature of photogenerated layers micro-Raman spectroscopy was described in this chapter as a possible method of characterization.

3.1 The effects of excimer laser on diamond films

In literature, it has been employed laser graphitization by excimer laser as an intermediate state that involves the evaporation of graphite and the ablation in order to generate patterns on diamond films. To make this purpose it is necessary a micrometer focusing to focus the radiation. This gives a single spot laser and by moving diamond with an automatical holder, it's possible to scanning the surface for micro-patterning [41].

Excimer laser sources operating at 308 nm (XeCl) [42] and 248 nm (KrF) [43], [44] have been explored; in these cases optical absorption occurs via

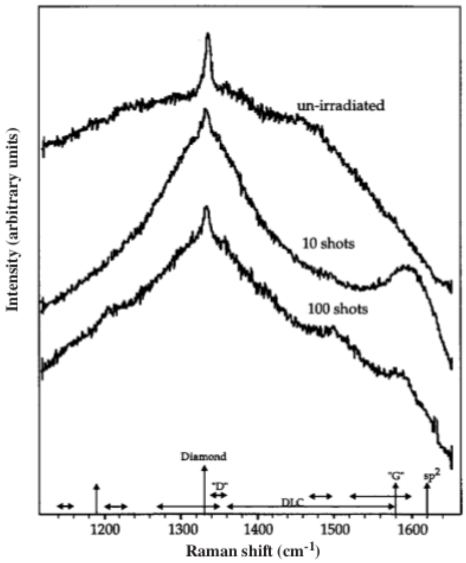

Fig. 3.1. Raman spectra of CVD diamond film modified by 193 nm (ArF) laser radiation at a fluence level of 2 J/cm^2 for a varying number of laser pulses (taken from [39]).

phonon modes, impurity bands, multiphoton or intraband processes [5]. However, since diamond has a bandgap energy of $\approx$ 5.5 eV, an excimer laser operating at 193 nm (ArF) can be more readily absorbed through band to band transitions. Excimer laser patterning of monocrystalline diamond with 193 nm radiation within various gaseous environments was first reported by Rothschild and co-workers [45]. Etch rates of around 50 nm per 15 ns pulse of 193 nm light were obtained at a laser fluence of 10 J/cm^2 which increased to 160 nm/pulse at 30 J/cm^2. A mechanism involving graphitization and subsequent sublimation was proposed; avoiding a graphitic residue required etching within a reactive gas environment such as chlorine. Thin film polycrystalline diamond excimer laser patterning in air has been studied by Johnston et al [46]. Etch rates of 2-4.5 nm per pulse were reported for a 193 nm laser fluence of 2.5 J/cm^2; the higher etch rates were achieved for films with the least diamond (sp^3) content. Formation of graphitic material followed by ablation of this phase was again considered as the origin of the material removal step; Raman microprobe analysis revealed the loss of the characteristic 1332 cm^{-1} diamond peak following exposure to 200 pulses of

193 nm radiation at 2.5 J/cm^2. In the work [39] it has been presented a detailed insight into the changes promoted in the remaining diamond substrate following 193 nm excimer laser promoted material removal. Film characterization by scanning electron microscopy (SEM), Raman scattering, Auger electron spectroscopy (AES) and electrical current-voltage measurements has been carried out. By these works we have collected the graphitization conditions in order to create graphitic layers on diamond and we have understood from Raman spectra taken on irradiated and unirradiated diamond that to avoid ablation process 10 ArF excimer laser pulses are necessary to graphitize the sample as we can see in Fig.3.1 in refer to [39], where in the spectrum for 10 excimer laser shots we see the G Raman band peaked around 1580 cm^{-1}, that give to us the proof about the presence of graphite on diamond surface.

3.2 Micro-Raman spectroscopy for different types of carbonaceous material

In any carbonaceous material, the presence of trigonally coordinated carbon (graphite) with different degrees of structural disorder is associated to the G band about 1580 cm^{-1}, to the D (disorder) band around 1350 cm^{-1} and to the G' band around 2720 cm^{-1}, with a shoulder at lower wavenumbers which is best defined in highly oriented pyrolytic graphite (HOPG), where it lies at 2680 cm^{-1}. The last feature is nearly absent in turbostratic t-graphite, where the stacking of graphene layers is rotationally random with respect to one another along the c-axis and the G' band is a single Lorentian, like in a graphene monolayer (ML). The difference between such G' bands with the same lineshape, still originating from these different materials, is the band FWHM value: 50-75 cm^{-1} is typical for t-graphite, while 25 cm^{-1} for graphene ML (Fig.3.2 given by ref. [47]). Graphene consists of sp^2 carbon hexagonal networks, in which strong covalent bonds are formed between two adjacent carbon atoms. The unit cell for monolayer graphene (1-LG) contains two carbon atoms, A and B, each forming a triangular 2D network, but displaced from each other by the carbon-carbon distance a$_{C-C}$ = 0.142 nm, as shown in Fig.3.3 (a). The 3D graphite structure corresponds to a stacking of the hexagonal networks of individual graphene layers in the direction perpendicular to the layer plane (c-axis) in an AB (or Bernal) stacking arrangement, in which the vacant centers of the hexagons on one layer have

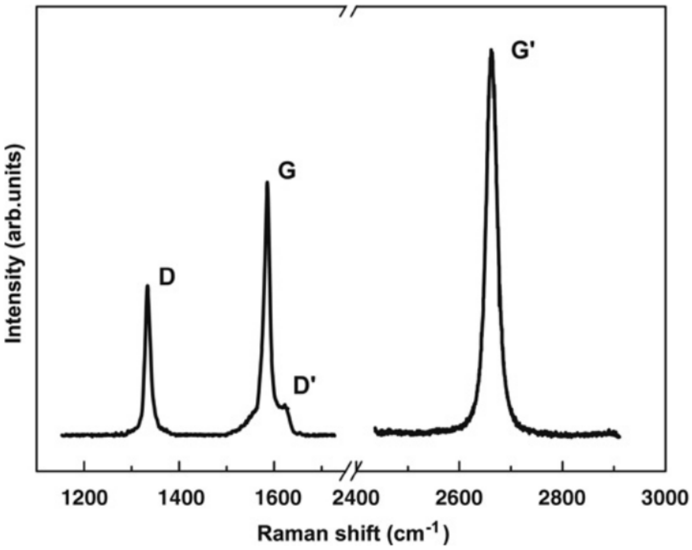

Fig. 3.2. Raman spectrum of a graphene edge, showing the main Raman features, the D, G and G' bands taken with a laser excitation energy of 2.41 eV (taken from [47]).

carbon atoms on hexagonal corner sites on the two adjacent graphene layers, as shown in Fig.3.3 (b). In graphite with AB stacking, the unit cell consists of four carbon atoms A_1 , A_2 , B_1 , and B_2 on the two layer planes shown in Fig.3.3 (b). The in-plane and c-axis lattice constants for graphite are a = 0.246 nm and c = 0.670 nm, respectively. Normally, the bilayer graphene samples obtained from the mechanical exfoliation of graphite exhibit an AB stacking arrangement, and therefore the number of atoms in the unit cell of bilayer graphene (2-LG) is the same as that for graphite, with four atoms per unit cell, as shown in Fig.3.3 (b) and (c). Trilayer graphene (3-LG) in turn contains three layers, two of which are like bilayer graphene and the third layer has atom A_3 over A_1 and atom B_3 over B_1 as shown in Fig.3.3 (d). Four layer graphene (4-LG) consists of the stacking of two unit cells of the type shown in Fig.3.3 (c), one stacked on top of the other.

In turbostratic graphite, denoted by 2D graphite, there is no stacking order between adjacent graphene layers and the interlayer spacing (> 0.342 nm) is larger than that for crystalline graphite (c/2 = 0.335 nm). The absence of stacking order between the graphene planes results in 2D graphite

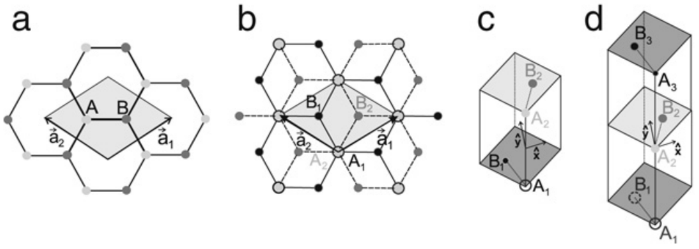

Fig. 3.3. (a) A top view of the real space unit cell of monolayer graphene showing the inequivalent atoms A and B and unit vectors $\mathbf{a}_1$ and $\mathbf{a}_2$. (b) A top view of the real space of bilayer graphene. The light/dark gray dots and the black circles/black dots represent the carbon atoms in the upper and lower layers, respectively, of bilayer graphene (2-LG). (c) The unit cell and the $\hat{x}$ and $\hat{y}$ unit vectors of bilayer graphene and (d) the same as (c) but for trilayer graphene.

having modified physical properties relative to 3D crystalline graphite. Crystalline 3D graphite is found in nature as a natural mineral, or is prepared from precipitants coming from steel-making and these flakes are called "kish" graphite.

3.3 Theoretical elements to evaluate the thickness of photogenerated graphite layer

In this section we propose a mechanism for photographitization of a free diamond surface to determine the quantum-kinetic rate of this process. The graphitization rate is close to zero if the activation energy of the graphitization process is taken as being equal to the binding energy of a carbon atom with the surface (i.e. equal to the sublimation energy of a carbon atom). On the contrary, if the activation energy is close to the energy of C-C bonds, the graphitization process may occur at a noticeable rate and be observed under 'relatively smooth' experimental conditions [40]. The temperature rise leads to a considerable increase in the graphitization rates. Our discussion is concerned with a combined thermal-photon mechanism for surface graphitization, when the transition of a carbon atom from a diamond state (sp^3-bonding) to a graphite state (sp^2-bonding) is affected by high temperature and simultaneous absorption of a laser photon. If the sample temperature

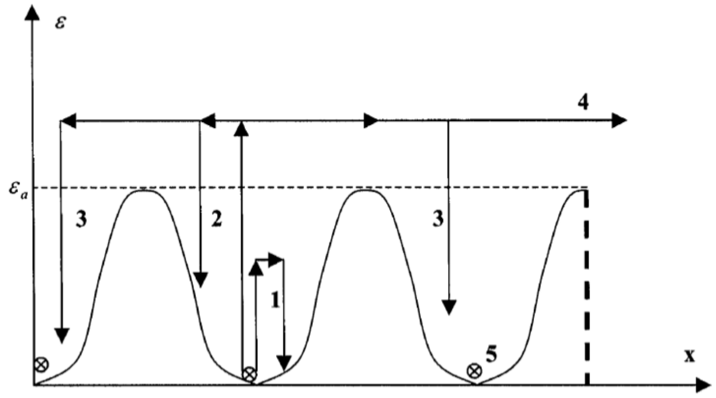

Fig. 3.4. Transitions of atoms in a near-surface potential relief. A *vertical dashed line* shows the position of the crystal surface. A *horizontal dashed line* indicates the activation energy or the potential barrier height. *Horizontal arrows* indicate possible spatial displacements of atoms. *Vertical arrows* denote excitation or relaxation of atoms in the lattice. Transitions "1" and "2" indicate excitation and relaxation of an atom in a potential well; these can lead to the formation of defects, or graphitization, of a given atom. Transitions "3" indicate diffusional jumps accompanied by the formation of interstitial defects or graphitization. Transition "4" indicates a sublimation transition from the surface or near-surface layers. "5" denotes a carbon atom in the equilibrium state.

is not very high, the rate of thermal graphitization is low and the graphitization process proceeds via successive quantum acts stimulated by light. Only those carbon atoms that individually absorb photons of energy $\hbar\omega$ can pass to the graphite state. The fact of metastability of 'diamond' atoms of carbon means that there is a potential barrier (ϵ_a) between the diamond and graphite states; the sp^2 state is characterized by a lower binding energy than the sp^3 state, and each of these energies indicates the bottom position of the corresponding potential well (Fig.3.4). This barrier must be overcome in the course of the graphitization transition. For different crystallographic orientations of the diamond surface, the activation energy (ϵ_a) has different values, e.g. $\epsilon_a\{110\} \approx 7.6$ eV/atom and $\epsilon_a\{111\} \approx 10.9$ eV/atom [48]. Very probably, the rate of thermal graphitization (R_0) follows a typical Arrhenius expression:

$$R_0 \approx \exp\left\{-\frac{\epsilon_a}{k_B T_0}\right\} \tag{3.1}$$

where ϵ_a is the activation energy per molecule and multiplying k_B (Boltzmann constant $= 8.6173324\times10^{-5}$ eV/K) with temperature T_0, we obtain the dependence of the rate from the temperature of diamond surface.

In addition to changes of energetic parameters during transition to the graphite state, a geometrical displacement of the carbon atom nucleus and a rearrangement of its electronic shells take place. In the laser field, the electronic shell rearrangement can be accompanied by a photon absorption. It is therefore possible to use the concept of the dipole moment (d) of the photon absorption during the graphitization transition. The dipole moment does not deal with the electron transitions from one level to the others inside an atom, but takes into account a change in the atomic state in the crystal lattice. We consider a graphitization act similar to that of the formation of a lattice defect [49]. If a carbon atom adsorbs the energy $\hbar\omega$, the value of thermal energy required for graphitization is decreased. Then it is needed that $\delta\epsilon \geq \epsilon_a - \hbar\omega$. It is evident that the probability of such a small fluctuation is higher, i.e. photostimulated graphitization can occur at higher rates than purely thermal graphitization. The rate of photographitization (R_1) is taken as:

$$R_1 \approx \exp\left\{-\frac{\epsilon_a - \hbar\omega}{k_B T}\right\} \tag{3.2}$$

Here $T = T_0$ or $T > T_0$, depending on whether the laser heating of diamond is small or not. By quantum-mechanical calculations, i.e. using any form of the time-dependent perturbation theory, we can have a better approximation for the rate of photographitization, given by [40]:

$$\begin{aligned} R_1 \approx & \frac{\sqrt{\pi}}{3}\frac{(2\pi M)^{\frac{3}{2}}a^3}{\hbar\omega}(dE_0)^2\sqrt{\epsilon_a - \hbar\omega} \\ & \times \left[1 + \frac{3Tk_B}{4(\epsilon_a - \hbar\omega)}\right] \\ & \times exp\left\{-\frac{\epsilon_a - \hbar\omega}{k_B T}\right\} \end{aligned} \tag{3.3}$$

where M is the atomic mass of carbon ($= 2 \times 10^{-23}$ g); a is the lattice constant of diamond structure ($= 3.57$ $\mathring{A}$ [50]), and d denotes the dipole moment ($= 7.69 \times 10^{-29}$ C $\cdot$ cm [51]) produced during the graphitization process. T represents the temperature distribution in the workpiece due to the irradiation energy; ϵ_a denotes the activation energy required in the graphitization process ($= 10.9$ eV/atom [48]); $\hbar\omega$ represents the photon energy absorbed by a carbon atom; E_0 represents the electric field induced by the electromagnetic wave produced in the laser system. We can define the graphitization probability (P_{photo}) of the diamond film multiplying Eq. (3.3) by t_d, i.e. the duration time of the laser pulse:

$$P_{photo} = R_1 \times t_d \tag{3.4}$$

Given the three-dimensional temperature rise distribution in the workpiece during the laser irradiation [51]:

$$\frac{\partial^2 T}{\partial x^2} + \frac{\partial^2 T}{\partial y^2} + \frac{\partial^2 T}{\partial z^2} = \frac{1}{\kappa} \frac{\partial T}{\partial t} \tag{3.5}$$

where κ denotes the thermal diffusivity of the workpiece (= 2.8 - 11.6 cm^2/s for diamond given to us by Diamond detectors Ltd company). These thermal properties are assumed to be independent from temperature. By the solution of Eq. (3.5) we have a temperature function that depends from spatial coordinates [51]. At this point we can substitute the obtained temperature in Eq. (3.4) and we can evaluate the graphite thickness photogenerated, because we consider the points where the temperature distribution gives values of graphitization probability in the interval between 0 and 1 [51]. In literature it has been demonstrated that the graphitization thickness varies from about 40 nm to about 85 nm as the laser fluence is elevated from 1.8 to 3.0 J/cm^2 [51].

Chapter 4

Excimer laser induced graphitization on diamond surface

In this chapter, we studied the structure and the morphology of a graphite layer induced on the surface of a polycrystalline thermal grade CVD diamond by focusing a pulsed excimer laser operating at KrF (wavelength 248 nm) and ArF (wavelength 193 nm) mixtures. By micro – Raman and PL spectroscopies, as well as Scanning Electron Microscopy (SEM) we reported the synthesis of a turbostratic t-graphite layer after irradiation with ArF laser. By contrast, irradiating with a KrF laser beam we obtained a disordered graphite layer with 10 laser shots, while 200 consecutive laser pulses resulted in target ablation. The experimental results obtained on this diamond type were used to graphitize in front and back another diamond type, a CVD diamond detector grade in order to create a device for nuclear applications.

4.1 Graphitization on CVD diamond thermal grade

In order to understand the graphitization process on diamond surface, we prepared an experimental setup to graphitize the sample and another to characterize the irradiated area as explained in section 4.1.1.

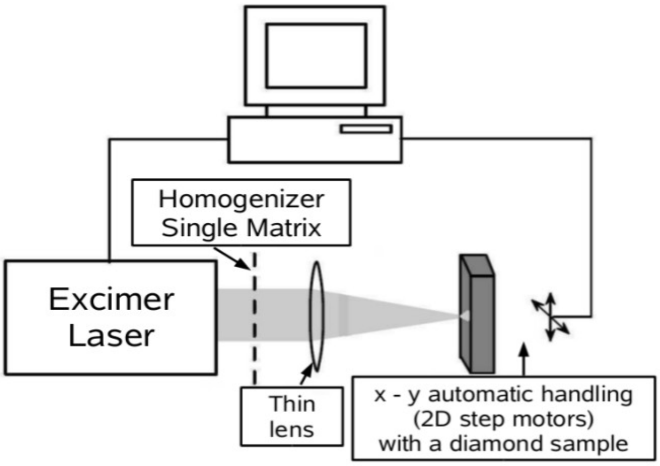

Fig. 4.1. Scheme of the setup for irradiating a diamond plate surface.

4.1.1 Experimental procedure

A polycrystalline thermal grade CVD diamond sample (10×10×0.2 mm^3) was laser irradiated on its surface using an excimer laser (Lambda Physik LPX305i), with two wavelength KrF (λ = 248 nm) and ArF (λ = 193 nm). The laser emitted 20 nsec long pulse with an energy of about 160 mJ/pulse at 10 Hz repetition rate. The laser beam with a transverse size of about 20×10 mm^2 was directed onto an homogenizer single matrix. The homogenized beam was then directly projected via a lens onto the sample placed on a computer assisted XY holder with a micrometric resolution. The focused image was a square of 3 mm^2 and the laser fluence at the sample of about 5 J/cm^2 with a top hat profile, as depicted in Fig.4.1. The diamond plate was processed in air and at room temperature. We have generated different patterns on diamond surface and for each zone we have chosen different laser parameters in order to check the different response. In Fig.4.2 are reported processed areas: the A area has been attained while the XY motion is stopped in a point, we focused KrF laser radiation and we fired 200 laser pulses. The same experimental procedure it was applied to the B area and to the B3 area, but for B area we have employed only 10 laser shots, while B3 area it was produced accidentally, because during the laser incidence the sample has jumped off from its holder.

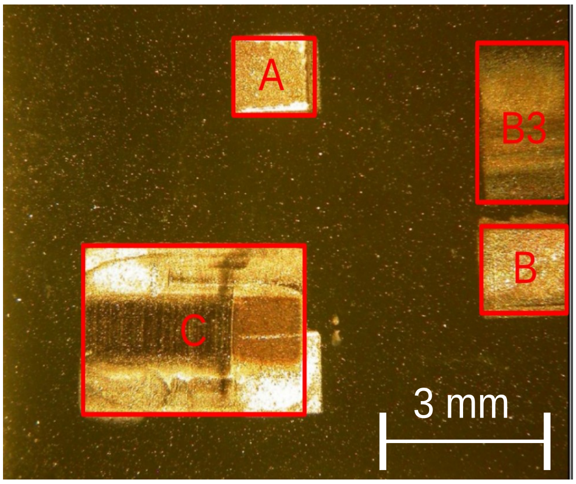

Fig. 4.2. Optical microscopy image of the polycristalline CVD diamond thermal grade plate with dimensions that are (10 × 10 × 0.2) mm. The black pads, selected with red rectangles, are photogenerated layers with different laser parameters as explained in the text.

Nevertheless we have, however, characterized this zone. Finally C area has been attained with the holder moving at a velocity of about 0.3 mm/s, while the laser spot was scanning the surface over 3 rows realizing a zone with a total area of about 9 mm^2. After that we have performed micro-Raman measurements on diamond and on graphite pads using an Ar$^+$ laser (wavelength 514.5 nm) which was focused by a 50× optical objective (Leica, Germany). At this excitation wavelength the numerical aperture is 0.75, which corresponds to a nominal spot diameter of 1 μm. The laser power was fixed at 1 mW at the sample surface, minimizing the possible radiation damage. The backscattered light was collected by the same objective and analyzed by a Renishaw inVia Raman Microscope equipped with a holographic Notch filter (cut-off at 100 cm^{-1}), a 1800 lines/mm diffraction grating and a thermoelectrically cooled RenCam CCD detector. The resolution was 0.5 cm^{-1} in the wavenumber range from 100 to 8000 cm^{-1}. Raman spectra were taken at different points of the graphite pad areas to evaluate spectra reproducibility. For A area we collected two Raman spectra at two different positions named KrFA1 and KrFA2, respectively. For B area we have the points KrFB1 and KrFB2, while for B3 area we have collected an only point

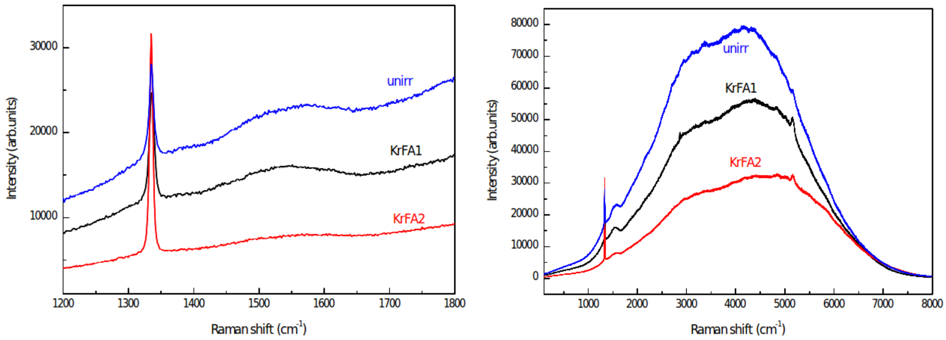

(a) (b)

Fig. 4.3. (a) Raman spectra taken at two different positions on A area (KrFA1 and KrFA2) and on unirradiated diamond; (b) PL spectra taken at two different positions on A area (KrFA1 and KrFA2), while blue line is PL spectrum on unirradiated diamond.

KrFB3. For C area we divided the stripe in two halves, the spectra were taken at two positions (points ArFC1 and ArFC2), located at the center of the stripe, at a distance of about one sixth of the stripe length from the external border on both sides. In addition, for the same points chosen in previous measurements, we have performed photoluminescence (PL) measurements on CVD diamond and on photogenerated pads. To confirm our findings we have carried out complementary scanning electron microscopy using a field ion microscope (Zeiss Supra-40) gently using a silver layer to increase sample conductivity, thus allowing for performing observations at higher magnifications on graphite.

4.1.2 Results and discussions

We recall here the main features for diamond in CVD films and for any carbonaceous material in the micro-Raman spectra. Diamond has a sharp peak centered at 1332 cm^{-1}. The peak width is associated to the random stress present, while the directional stress results in peak shifting, or splitting. In any carbonaceous material, the presence of trigonally coordinated carbon (graphite) with different degrees of structural disorder is associated to the G band about 1580 cm^{-1}, to the D (disorder) band around 1350 cm^{-1} and to the G' band around 2720 cm^{-1}, with a shoulder at lower wavenumbers which

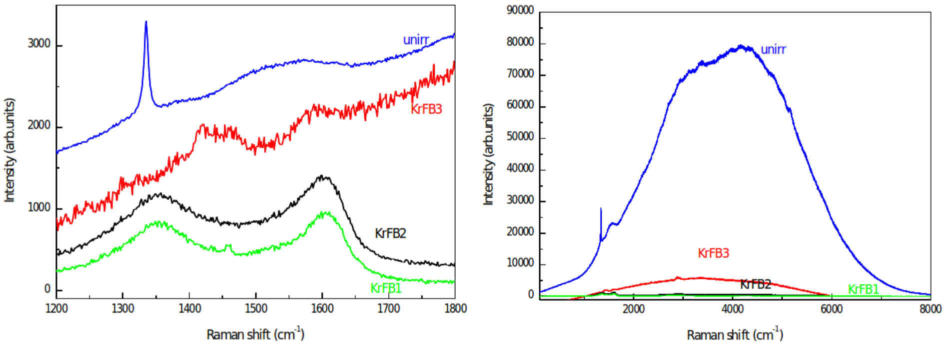

(a) (b)

Fig. 4.4. (a) Raman spectra taken at two different positions on B area (KrFB1 and KrFB2), on B3 area (KrFB3) and on unirradiated diamond; (b) PL spectra on B area, B3 area and on unirradiated diamond.

is best defined in highly oriented pyrolytic graphite (HOPG), where it lies at 2680 cm^{-1}. The last one is nearly absent in turbostratic t-graphite, where the stacking of graphene layers is rotationally random with respect to one another along the c axis and the G' band is a single Lorentian, like in graphene monolayer. The difference between such G' bands with the same lineshape, still originating from these different materials, is the band FWHM value: 50-75 cm^{-1} is typical for t-graphite, while 25 cm^{-1} for graphene monolayer ML [47]. A further feature of CVD diamond is a high wavenumber contribution from vibronic centers which generates the photoluminescence (PL) intense band extending from about 3000 to about 7000 cm^{-1}, with a broad maximum around 5000 cm^{-1} [52].

A representative micro-Raman spectrum from our unirradiated diamond [blue curve in Fig.4.3 (a)] shows a narrow peak centered at 1335 cm^{-1} (FWHM, 9 cm^{-1}), and a broad G band extending from about 1450 to 1650 cm^{-1}, with a maximum around 1570 cm^{-1}; both these features grow up from a luminescence background. The G band is very likely due to the presence of graphitic carbon forms in CVD diamond [53]. At higher wavenumbers a complete spectrum of the unirradiated material is reported [blue curve in Fig.4.3 (b)], where the broad, intense PL band is the dominant feature; we observe a very weak and characteristic feature at about 3750 cm^{-1}, attributed to the

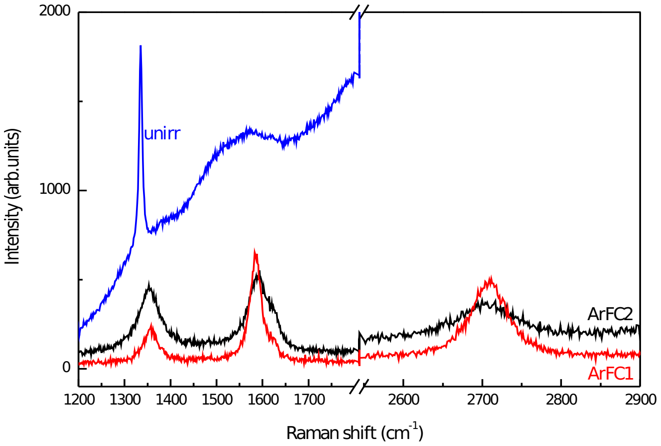

Fig. 4.5. Raman spectra taken at two different positions on C area (ArFC1 and ArFC2) and on unirradiated diamond.

neutral (2.156 eV) charge state of a vacancy trapped at a single substitutional nitrogen which was accidentally incorporated in the material during the synthesis procedure [54]. Given the large wavenumber separation and intensity difference between micro-Raman and PL features in all recorded spectra, we separately discuss both regions for our samples. From A area (Fig.4.2), we collected two micro-Raman spectra at different positions, as shown in Fig.4.3 (a) (KrFA1 and KrFA2, respectively). Such spectra display the same features as that of unirradiated diamond, this, likely, happens because we have fired 200 consecutive laser pulses. It's known that KrF laser can graphitize diamond surface, but continuing the irradiation, the laser can be absorbed from graphite, forcing it to evaporate [40]. In the same spectrum the G band maximum shifts at about 1545 cm^{-1} as evident in the spectrum of the point KrFA1, the intensity lowers in the point KrFA2 while the diamond peak height (1335 cm^{-1}) increases. It well known that when the amount of graphite decreases (G band) in diamond film correspondingly diamond peak increases in intensity [53]. In the same way the PL bands [Fig.4.3 (b)] keep the shape unaltered and show a consistent intensity reduction. In B area we chose two points (KrFB1 and KrFB2) that lie in the lower and upper borders of the irradiated area B, while we chose a single point (KrFB3) in B3 area. Micro-Raman spectrum of the point KrFB3, shown in Fig. 4.4 (a), exhibits evident features of disordered graphite: the bands at about 1350 cm^{-1} (D) (very weak) and 1590 cm^{-1}(G), emerging over a luminescence background. Both the bands are most evident in the spectra of points KrFB1 and KrFB2. A further broad band, centered around 1430 cm^{-1} with a component around 1450 cm^{-1}, is the dominant feature in the spectrum of point B3. Both bands appear as weak features even in the spectrum of point B1: the band at 1430 cm^{-1} was attributed to chaoite, a metastable carbon phase resulting from heavily shocked graphite [55]. Our laser irradiations provide the shock wave conditions able to form such metastabile carbon phase, while the opposite phase transition, from graphite to nano-diamond and to chaoite, was observed under energetic cluster beam bombardment [56]. Moreover the band at 1450 cm^{-1} could be assigned to transpolyacetylene, provided some hydrogen is present in the irradiated material [57]. The intensity of the PL band is dramatically reduced for KrFB3 point on respect of unirradiated diamond and it practically disappears in KrFB2 and KrFB1 as shown in Fig.4.4 (b). Micro-Raman spectra of C area are shown in Fig. 4.5 which report dramatic changes with respect to both unirradiated diamond and the other areas. The diamond features disappear, the G band around 1580 cm^{-1} is well defined, becoming sharper and relatively more intense when the D band at 1360 cm^{-1} is less pronounced for ArFC1 spectrum. Instead a second order G' band appears centered at about 2720 cm^{-1} with a single Lorentian lineshape and a FWHM of about 70 cm^{-1} for ArFC1 and about 110 cm^{-1} for ArFC2, while it's not possible to detect a PL band for C area. All micro-Raman measurements point out that laser irradiation is effective to induce structural changes from diamond to disordered graphite (B and B3 areas) or to t-graphite (C area). To confirm the aforementioned findings we performed scanning electron microscopy observations. In Fig.4.6 we show the surface of B area. At low magnification [Fig.4.6 (a)] the laser-irradiated zone looks quite homogeneous with some scattered sized 0.2-0.5 micron debris; at higher magnification [Fig.4.6 (b)] the surface appears a homogeneous distribution of irregularly shaped particles with average size around 20-30 nm, while in Fig.4.6 (c), where SEM observation for unirradiated diamond surface is reported, we don't see these irregularly shaped particles. Pictures taken from C area are showed in Fig.4.7, for which increasing the magnification we observe at first a surface homogeneously modified by the laser radiation [Fig.4.7 (a)]. The details of a randomly oriented distribution with irregularly shaped flakes, partly protruding outwards from the surface becomes evident and constitutes a signature of t-graphite [Fig.4.7 (b)]; at still higher magnification

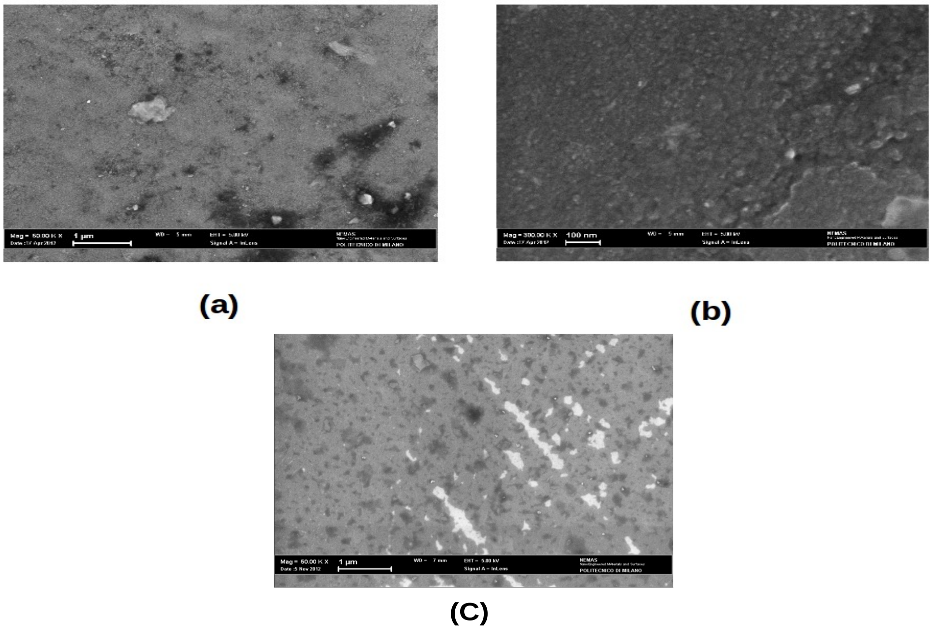

Fig. 4.6. SEM micrographs from B area at increasing magnification from (a) to (b). In (c) unirradiated diamond surface is reported.

[Fig.4.7 (c)] the flakes are even more clearly visible and their average size can be estimated around 20-30 nm. Such a morphology was observed only in C area.

4.2 Graphitization on CVD diamond detector grade

In order to make a diamond device for nuclear applications we graphitized in front and back an high quality Chemical Vapor Deposition (CVD) diamond. The sample was an undoped synthetic detector grade polycrystalline diamond with a thickness of 300 μm after chemical polishing and laser cutted to a size of 0.5×0.5 cm^2. Chemical polishing was given by 15 minutes boiling diamond sample in a chromic acid powder dissolved in H_2SO_4 followed by 5

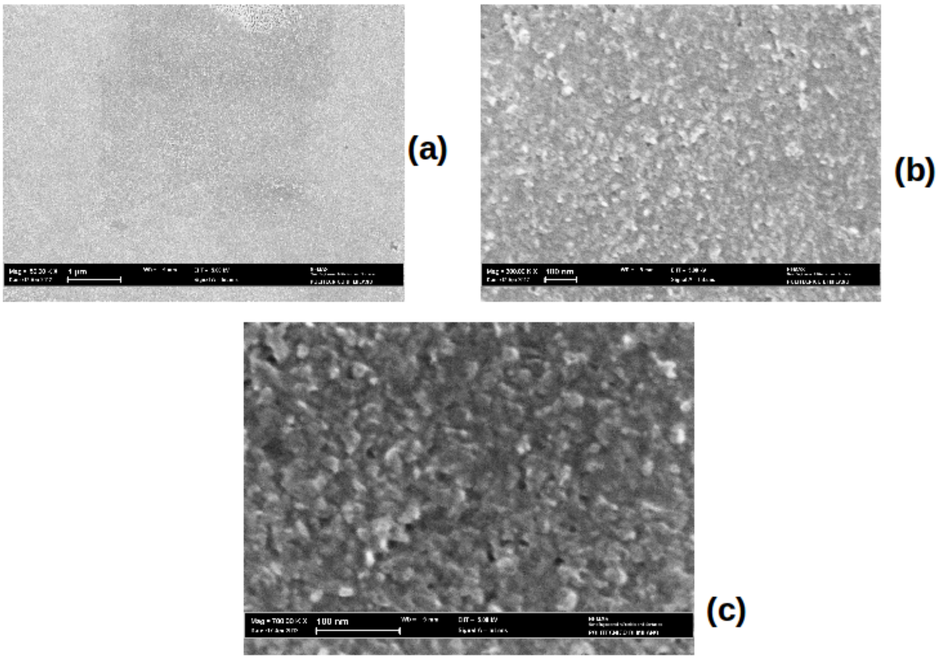

Fig. 4.7. SEM micrographs from C area at increasing magnification from (a) to (c)

minutes boiling in piranha solution (50:50 H_2SO_4 and H_2O_2). The next step was the immersion of the sample in a boiling solution: 4:1:1 deionized (DI) Water + HCl + H_2O_2 for 1 minute. Finally the sample was blowed dry in ultra dry N_2 gas for 7 minutes $\approx$ 40 watt plasma in 50 cubic in chamber. In each case when we changed the boiling solution, prior to immerge the sample, we made a DI water rinse by ultrasonic bath. After chemical polishing diamond device was prepared with an experimental procedure analogous to that described in section 4.1.1, i.e. we irradiated in front (grow side) and back (seed side) diamond surfaces with the ArF excimer laser (Lambda Physik LPX305i) at 193 nm. In this way graphite electrodes with an area of about 3×3 mm^2 were made on both sides of diamond by using the automatic handling to scan the surfaces with a velocity of about 0.3 mm/s [see Fig. 4.8 (a)]. In first analysis we verified the strong mechanical resistance about graphitic layers, because we couldn't remove any graphite piece by mechanical instruments, such as cutters or knives. In second analysis micro-Raman

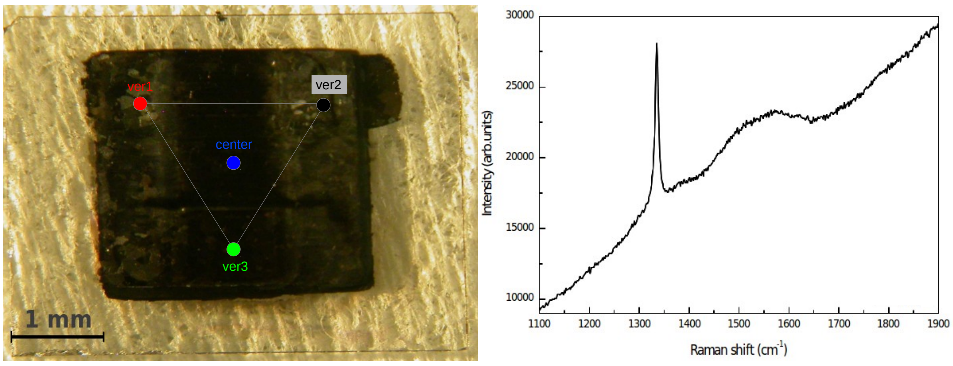

(a) (b)

Fig. 4.8. (a) Optical microscopy image of the polycrystalline CVD diamond detector grade after laser treatment. The black pad at the center of the device is the photo-generated graphite electrical contact. The coloured circles represent a scheme of points in which we performed micro-Raman and SEM characterizations. The graphitised sample is turned by the grow side surface as explained in the text; (b) Micro-Raman spectrum of unirradiated CVD diamond detector grade.

and photoluminescence (PL) measurements, SEM images, were taken using the same experimental setup described in section 4.1.1 to characterize the irradiated area. Micro-Raman and PL spectroscopy was collected in front and back at different points, i.e. at the vertexes of a triangle and at the center in order to warrant the reproducibility of the measures in refer to Fig. 4.8 (a), while SEM images approximatively at the center of the irradiated pad for both surfaces. A preliminary visual and optical microscopy observation indicates that throughout them thin surface layers of carbonaceous material were photon modified.

A representative micro-Raman spectrum from our unirradiated diamond [Fig. 4.8 (b)] displays a narrow peak centered at 1335 cm^{-1} (FWHM, 8 cm^{-1}), and a broad G band extending from about 1450 to 1640 cm^{-1}, with a maximum around 1565 cm^{-1}; both these features grow up from a luminescence background. This spectrum was taken from the front face of the sample and it is identical to a spectrum taken from the back face of the sample (not reported). The same analysis made on irradiated area is reported and we can see in Fig. 4.9 micro-Raman spectra. For front side surface [Fig. 4.9 (a)] the general information is that laser irradiation brings about diamond

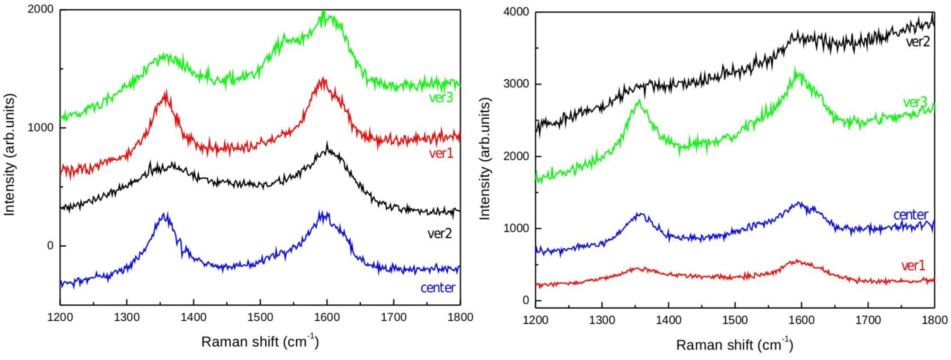

(a) (b)

Fig. 4.9. Micro-Raman spectra taken at four different positions on graphitised pad for detector grade CVD diamond in refer to Fig. 4.8, (a) is for grow side surface (front) and (b) for seed side (back).

graphitization, as indicated by the presence of the G and D bands; yet the G band extends up to about 1650 cm^{-1}, peaking between about 1590 and 1600 cm^{-1}: this important blue-shift is likely to be associated to the presence of a considerable fraction of disordered diamond, sp^3 coordinated [58]. When we look at the details of the different micro-Raman spectra we see that the spectrum taken at vertex 3 has a shoulder at about 1540 cm^{-1} that appears in the other spectra as a weak feature around 1532 cm^{-1} whose intensity is scales inversely with the D/G ratio of the considered spectrum. As to the D band, in all spectra it is centered at about 1350 cm^{-1}: this is expected in micro-Raman spectrum of a disordered graphitic carbon when green excitation light is used, as in our measurements. From Fig. 4.9 (b) Raman G and D bands are evident; G bands are very broad, peaked at about 1590 cm^{-1}, with a shoulder at about 1630 cm^{-1}, while D bands are centered around 1360 cm^{-1}. The overall information from Raman spectroscopy of the back face of the sample agrees with that from the front face, namely that under this type of laser irradiation detector grade CVD diamond is converted to graphitic, strongly disordered.

We discuss now the spectral features of the front and the back irradiated sample faces about photoluminescence (PL). In Fig. 4.10 (a) is displayed the collection of PL spectra taken at the four selected points on the front side

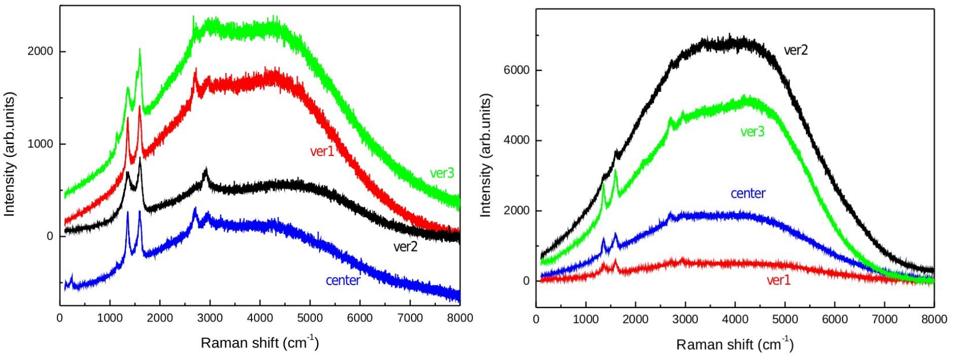

(a) (b)

Fig. 4.10. PL spectra taken at four different positions in refer to Fig. 4.8, (a) is for grow side surface (front) and (b) for seed side (back).

of the sample in refer to Fig. 4.8 (a). We observe that the irradiation effect was not uniform cross the irradiated area: although PL intensity is low in all spectra, it is even lower at the center and at vertex 2 with respect to vertices 1 and 3. The second order Raman G' band, centered at about 2720 cm^{-1}, is weak. While about back irradiated side of the sample, PL spectra in Fig. 4.10 (b) again show that the effect of laser irradiation was not uniform: at vertices 2 and 3 the intensity of PL spectra is high and comparable to what is expected from diamond, while it is strongly reduced at vertex 1 and at the center of the sample. Also in this set of spectra second order Raman features at about 2720 cm^{-1}, are weak.

In Fig. 4.11 are displayed SEM micrographs taken on the front and back faces of the sample, approximately at the center position. Low magnification pictures show that the surface morphology of the sample is uniform across the whole irradiated surface on both faces. From both Fig. 4.11 (a) and (c), taken at the same intermediate magnification (20000 x) the surfaces appear stepped, with an irregular, dense distribution of nanoparticles, about 200 to 400 nm in size, partly protruding outwards. The bigger ones are located mostly in the step regions. In Fig. 4.11 (b), that was taken from a portion of the area imaged in Fig. 4.11 (a) for a magnification of 50000×, the spongy nanoparticle morphology is more evident.

For unirradiated area an optical profile image was given by Diamond

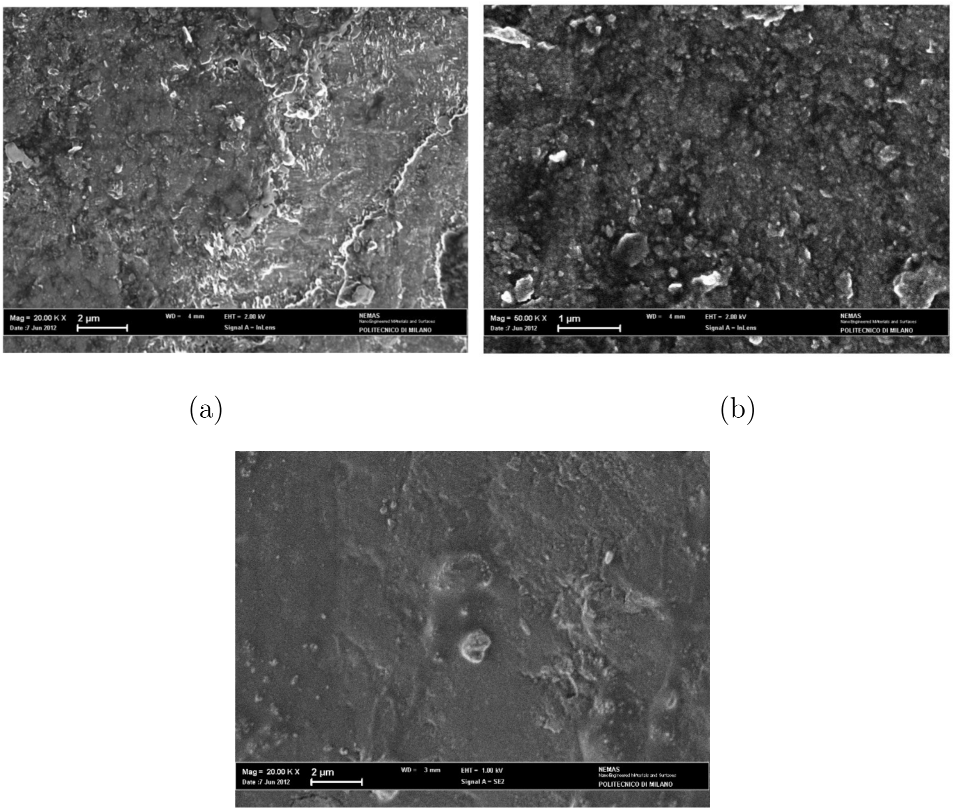

(a) (b)

(c)

Fig. 4.11. SEM micrographs taken at the center of the irradiated area in refer to Fig. 4.8 (a).

Detectors Ltd company (Fig. 4.12). This image was taken from the front face of the sample and it is identical to the image taken from the back face of the sample (not reported). They used a Wyko NT9100 Optical Profiling System that employed coherence scanning interferometry, also known as white-light interferometry, white-light confocal, or vertical scanning interferometry to produce high quality three-dimensional surface maps of the object under test with a sub-nanometer vertical resolution at all magnifications. From a confront of the images about irradiated and unirradiated diamond we can

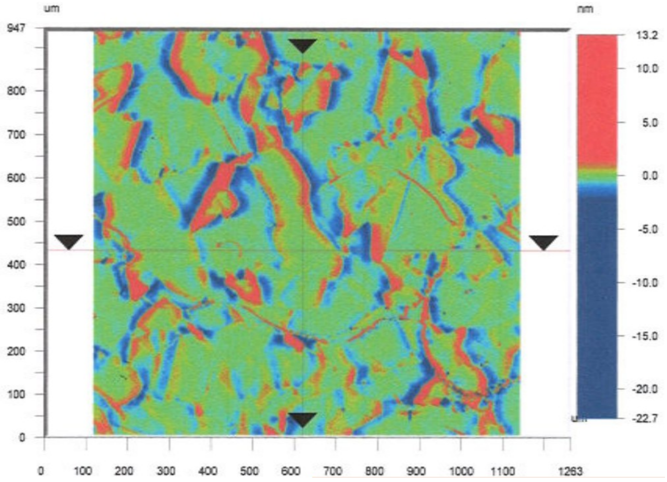

Fig. 4.12. Optical profile image for CVD diamond detector grade on unirradiated surface.

see that laser irradiation produce changes about the structure of the sample surfaces.

4.3 Differences between two different diamond types

In order to understand the differences between CVD diamond detector grade and thermal grade, transmission measurements have been performed on unirradiated sample by using for UV/Visible/NIR a PERKIN ELMER Spectrometer Lambda 900 and for FT-IR a PERKIN ELMER Spectrum 2000 in this way an only transmission spectrum was obtained in the range that go from 0.2 μm up to 30 μm for each diamond sample (Fig. 4.13).

In literature graphitization process on diamond surface by ArF laser is reported [39], but the authors don't see t-graphite, i.e. don't see G' band in Raman spectra, but only D and G bands that is the same result we obtain for CVD diamond detector grade. This is due to very probably at the different absorption properties of the polycrystalline thermal grade CVD diamond sample, because other diamond types [50] have an UV/Visible/NIR and FT-IR transmission spectrum with a transmission of the 70% that go from the UV

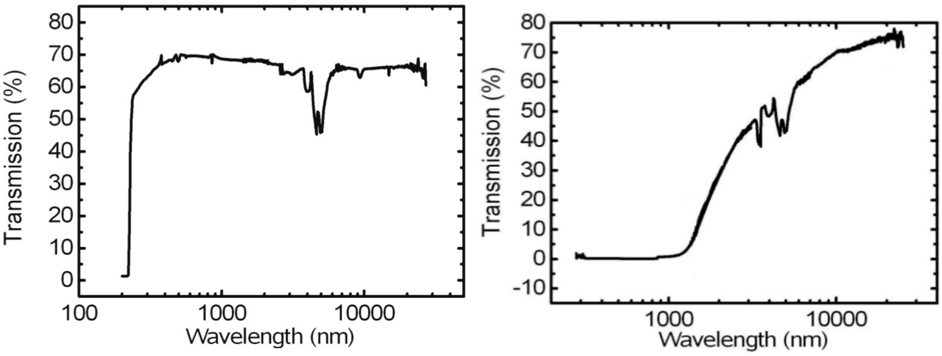

(a) (b)

Fig. 4.13. UV/Visible/NIR and FT-IR transmission spectra for polycrystalline detector grade CVD diamond (a) and for polycrystalline thermal grade CVD diamond (b).

(225 nm) up to the far infrared. Only minor absorption bands exist resulting from two phonon absorption [59] between 2.5 and 6.5 μm. This characteristic is also evident in our unirradiated diamond detector grade sample [Fig. 4.13 (a)], but for diamond thermal grade transmission spectrum is quite different [Fig. 4.13 (b)]. Probably this is due to the presence of graphitic states in diamond bulk that explains the absorption of thermal grade sample in visible range. When we irradiate diamond thermal grade plate by ArF laser radiation, this focused laser beam is absorbed by diamond and graphitic states, in this way we can produce t-graphite layers because this transition is energetically favoured.

Chapter 5

Diamond detectors with graphitic electrical contacts

We created three radiation detection devices from a plate of high quality polycrystalline CVD diamond. The first was fabricated with nano-graphite electrical contacts on both diamond surfaces, by front and back irradiation with a 193 nm ArF excimer laser. We measured the electrode electrical resistance and evaluated a graphite resistivity of about $10^{-5}\Omega\cdot$m. The ohmic nature of the contact graphite/diamond is established measuring the current-voltage characteristic that it is described by a linear behaviour up to 90 V, by a Space Charge Limited (SCL) regime above 100 V and below 300 V, and by a Trap Filled Space Charge Limited (TFSCL) regime above 300 V. Finally, we investigated the device response in counting mode to a 60 Co γ-rays source and to a 120 GeV proton beam proving its capability to work as a fast nuclear radiation detector. The second was a micro-strips detector made by micro-focusing the same laser beam at 193 nm for which we carried out the resistance measurements on the graphite electrodes and the capacitances for diamond bulk and surface. The third was a three strips detector for which three strips were made with the same geometrical structure, but different chemical composition and structure, in order to evaluate the differences in response for these three different materials.

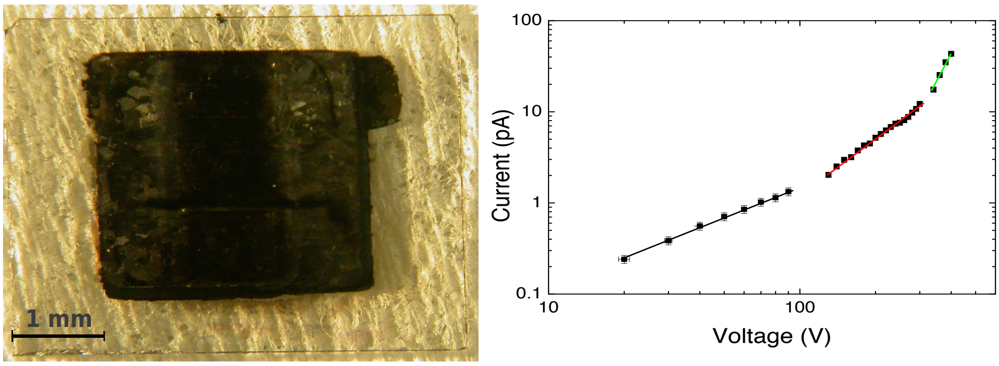

(a) (b)

Fig. 5.1. (a) Optical microscopy image of the polycrystalline CVD diamond detector grade plate of $(5 \times 5 \times 0.3)$ mm^3 size after laser treatment. The black pad at the center of the device is the photo-generated graphite electrical contact created on diamond sample surfaces; (b) Current-voltage characteristic of the graphitised device in log-log scale. The superimposed fits correspond to power law curves $\mathrm{I} \propto \mathrm{V}^k$ where the power law indexes k, for the three different voltage regimes, are reported in Table 5.1.

5.1 Pad detector

Pad detector is a device with two graphite electrodes of 3 mm^2 created in front and back of a CVD diamond plate surface. We introduced it in section 4.2, but in this one we analyse its capability to work as a fast nuclear radiation detector and study its response before and after radiation damage.

5.1.1 Electrode electric resistivity

In order to test the conductive properties about graphite electrodes electric resistance measurements were performed on them by a common digital multimeter KDM-350 CFT. We collected 100 measurements, along the horizontal and vertical directions, and we obtained a mean value for all cases of about 40 Ω. Consequently, we can assume that the irradiated area was uniform, despite three graphitic vertical bands, related to the laser scanning, are visible in Fig. 5.1 (a). In order to evaluate the sheet resistance R_S for graphite

Voltage range	Power law index (k)
0-90 V	1.13 ± 0.02
90-300 V	2.00 ± 0.03
300-400 V	5.60 ± 0.36

Table: 5.1. Power law index k of the current-voltage characteristic showed in the plot of Fig. 5.1 (b) for the three different voltage regimes.

layers, we applied the Van Der Pauw method ([60]) given by the equation:

$$e^{-\pi R_{vertical}/R_S} + e^{-\pi R_{horizontal}/R_S} = 1. \tag{5.1}$$

Assuming the condition $R_{vertical} = R_{horizontal} = R = 40\Omega$, we can calculate the sheet resistance R_S:

$$R_S = \frac{\pi R}{ln2} = \frac{\rho}{t}, \tag{5.2}$$

where the third member of Eq. 5.2 is given by the definition of sheet resistance, i.e. t is the sheet thickness of the graphite pad and ρ is the graphite electrical resistivity. We assume that t is about 60 nm for a laser fluence of about 3 J/cm^2 in refer to [51] and estimate ρ from Eq. 5.2 that is about 10×10^{-6} Ω·m quite consistent with graphite resistivity along the perpendicular direction of c-axis 9.8×10^{-6} Ω·m [61].

5.1.2 Current-Voltage characteristic of the device

Current-Voltage characteristic of the device was made in order to measure diamond bulk resistivity. The device was biased by fixing the sample between two gold arms soldered to a coaxial SMA connector. A small anodized aluminum box was used as a Faraday shield to avoid any type of electrical noise during dark current-voltage (IV) measurements. We employed the instrument 6487 Keithley pico-ammeter/voltage source with voltages ranging from 0 to 400 V. The plot of Fig. 5.1 (b) shows the measured IV characteristic in log-log scale that was made both for positive and negative voltage values for which the experimental cyclic measurement give to us a set of overlapping points. By this evidence we proof that no hysteresis is presented, but we see three different conduction mechanisms characterized by three different power law relations between current and voltage $I \propto V^k$ (see Table 5.1).

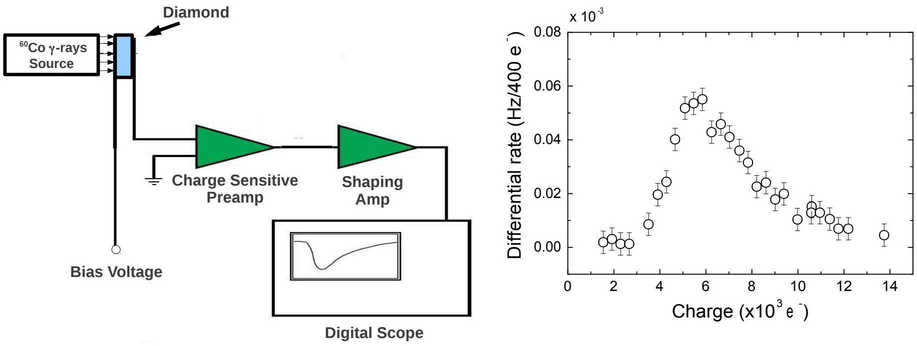

(a) (b)

Fig. 5.2. (a) Experimental setup used to measure diamond detector responses under γ-rays radiation and 120 GeV proton beam; (b) Charge distribution from a γ-rays (^{60}Co source) measured by diamond detector with laser-graphitised electrodes. The data correspond to an applied high voltage of 300 V.

For voltages up to about 90 V the relation between I and V is approximately linear with a measured power index k=1.13±0.02 (Table 5.1). This behaviour can be explained assuming that the graphite/diamond interface behaves like a metal/semiconductor interface with an electrode work function smaller than the semiconductor work function. The diamond acts like a semiconductor with a band gap of about 5.47 eV and very high bulk electrical resistance. From the theory of Schottky contacts this gives a barrier free electrode interface and we obtain an Ohmic contact [62]. In this case electrons are injected from the external circuit by one electrode and collected by the other one. For small applied voltages, a space charge region extends only for a limited distance inside the insulator and the electrons move in the conduction band. In this case, the conduction process is ruled by the diamond bulk resistivity ρ_d, that can be calculated by the Ohm's law $V = I\frac{\rho_d L}{S}$, where L and S are the diamond sample thickness and the electrode surface, respectively. In this regime, we found a resistivity $\rho_d \propto 10^{14}\Omega \cdot \mathrm{cm}$.

However, increasing further the electric field, the two space charge regions start to overlap each other extending through all the insulator and the conduction process becomes Space Charge Limited (SCL). This happens for high voltages from 120 V to 300 V, where the relation between I and

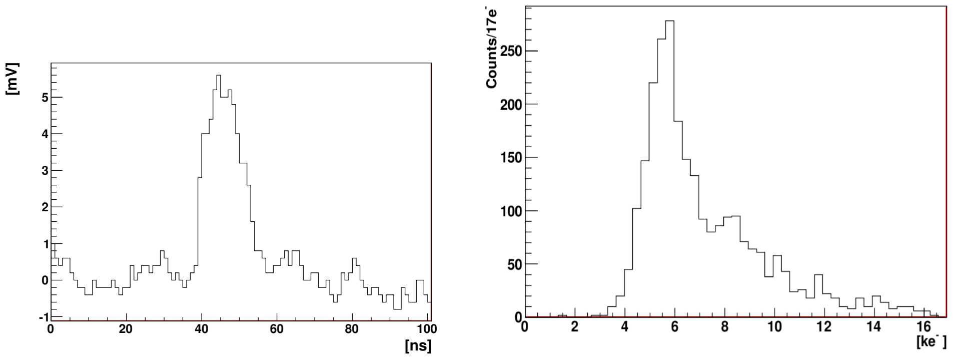

(a) (b)

Fig. 5.3. (a) Typical time profile of the signal induced on diamond detector with laser-graphitised electrodes by a 120 GeV proton; (b) Charge distribution from a 120 GeV proton beam measured by diamond detector with laser-graphitised electrodes. The data correspond to an applied high voltage of 300 V.

V is quadratic with a measured power index k=2.00±0.03 (Table 5.1), as predicted by Mott and Gurney (1948, see ref.[63]) for a trap-free insulator.

For higher voltages from 300 V to 400 V the dependence of I with respect to V is very rapid, with a measured power index k=5.60±0.36 (Table 5.1). Rose (1955, see ref.[63]) has derived a Trap Filled SCL conduction mechanism described by the following relation:

$$I \propto V^{(T_e/T+1)}, \tag{5.3}$$

where T is the bulk temperature and T_e is a characteristic temperature describing the exponential distribution of defected states localized near the edges of valence and conduction bands. We performed the measures at room temperature and from the value of power index k we evaluated a T_e of about 1686 K. In fact, the polycrystalline structure of diamond can't be neglected because the grain boundaries or defects inside the grains destroy the long-range order of the lattice.

5.1.3 Radiation detection

Diamond radiation detectors are generally designed as a parallelepiped solid state ionization chamber in two main configurations: with electrodes front and back (called "Sandwich" configuration) or interdigitated electrodes on the same surface.

A charged particle passing through diamond releases in average 13 eV to produce an electron-hole pair ([1]). The produced pairs are separated in presence of an electric field. Electrons drift towards the positive electrode, while holes drift in the opposite direction. As the free carriers move, a charge is induced on the electrodes, which can be integrated by a charge-sensitive preamplifier [2].

To verify that our device is capable to detect a signal due to the drift of a charge generated by ionizing radiation, we measured the pulse height induced by Compton scattered electrons produced by photons emitted from a low intensity ^{60}Co γ-rays source. For the measurement we used the experimental set-up shown in Figure 5.2 (a). The induced charge was integrated by a low noise charge preamplifier (ORTEC 142A) followed by a shaping amplifier (Ortec 450) and the output signal was recorded by a digital scope. We converted the measured pulse height V_s in the collected charge Q_c by applying an electric pulse $V_{cal,inp}$ of known amplitude to the charge preamplifier calibration capacitance C_{cal} and measured the corresponding output pulse height $V_{cal,out}$:

$$Q_c = V_s \frac{C_{cal} V_{cal,out}}{V_{cal,inp}}. \tag{5.4}$$

The plot in Figure 5.2 (b) shows the charge distribution of the source measured by the graphitised detector for an applied voltage value of 300 V, corresponding to an internal electric field of 1V/μm.

We also measured the detector response for a 120 GeV proton beam produced at the Fermilab Test Beam Facility (FTBF) [64], which corresponds to a minimum ionizing particle and is expected to release about 36 e-h pairs/μm ([1]). Figure 5.3 (a) shows a single recorded pulse acquired by a 1 GHz bandwidth oscilloscope due to the passage of a 120 GeV proton. For these measurements the amplification chain was different from the previous one. The signals were amplified by a fast 100 MHz bandwidth charge sensitive preamplifier having a gain of 8mV/fC, a rise time of about 3 ns and a fall time of about 8 ns. The signal shape in Figure 5.3 (a) is dominated by the fast charge sensitive preamplifier response, because the expected charge drift time is about 1 nsec. In fact, the drift time is given by the charge collection distance, divided by the carrier drift velocity, which are about 100 μm and 100 μm/ns, respectively, according to the supplier informations for diamond.

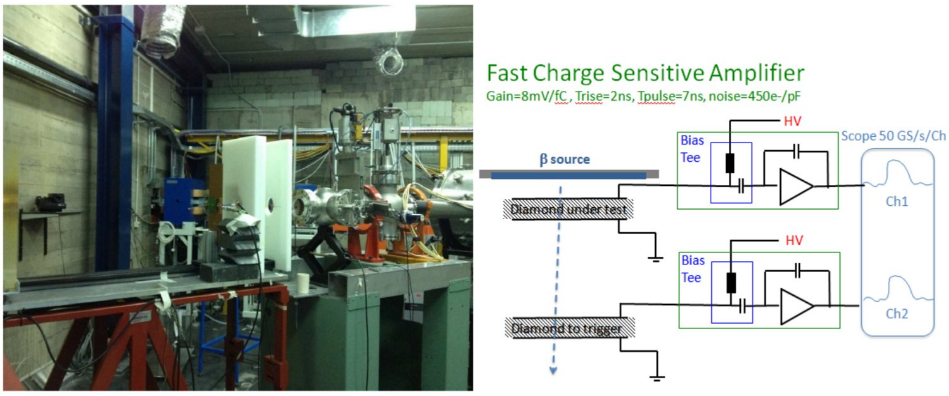

(a) (b)

Fig. 5.4. (a) Setup in the experimental area for the 62 MeV proton irradiation at INFN Laboratori Nazionali del Sud (Catania, Italy); (b) β source experimental setup with fast charge amplifiers to study fast detector response.

In order to match the oscilloscope sensitivity, a 1.5 GHz bandwidth voltage amplifier, having a gain of a factor 100, was used. The voltage amplifier is fast enough to avoid signal deformation and the signal in Figure 5.3 (a) is already rescaled by its voltage gain. The charge distribution of the 120 GeV protons is shown in Figure 5.3 (b). Comparing Figures 5.2 (b) and 5.3 (b) we see that the peak for both spectra correspond to a charge of about 5,400 electrons. We realized that the measured gamma and proton peaks in the spectra are just an artifact of the oscilloscope threshold used to trigger the signal and reduce the noise contributions. However, we can conclude that our device is capable to work as radiation detector in counting mode. Anyway, we cannot exclude that a sizable amount of charge collection inefficiency is present due to traps in diamond bulk or in proximity of graphite/diamond interface.

5.1.4 Radiation damage

In this section we complete the study about pad detector based on diamond detector grade type by studying radiation damage of polycrystalline diamond in terms of time response. For this purpose the device was glued to a pc-

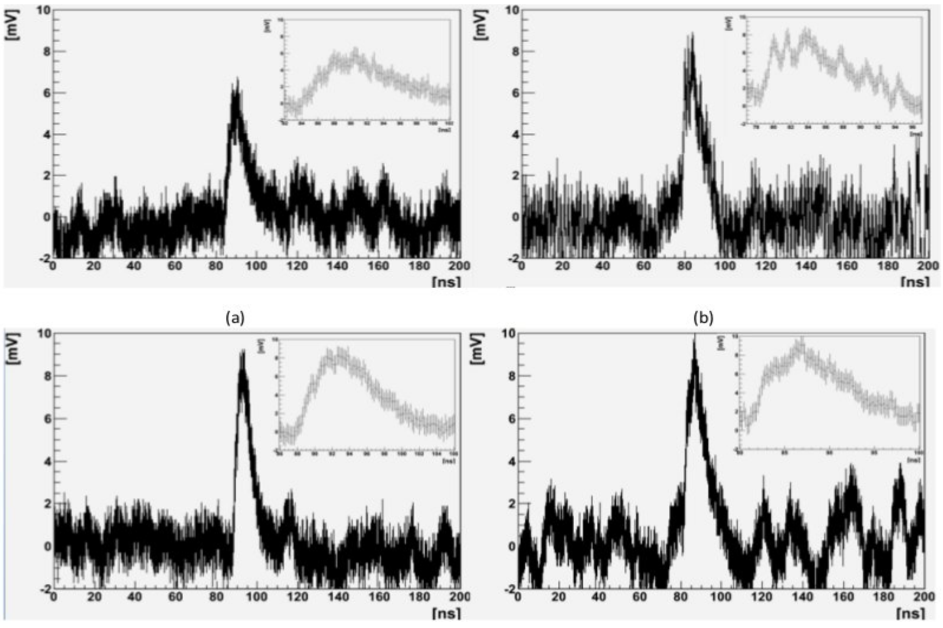

(a) (b)

(c) (d)

Fig. 5.5. Time response to a β source for a commercial diamond detector before (a) and after (b) protons irradiation and for the graphitized diamond detector before (c) and after protons (d). The insets are zooms of the peaks.

board having a central hole at Università del Salento and in order to have a comparison for the response another diamond device were used as reference detector respect to graphitized detector. This new device has made with the same diamond quality that we employed to make the pad detector in this thesis work, but the electrodes were deposited (DLC/Pt/Au) on both surfaces of the plate (front and back) according to the ref. [65] and packaged in an aluminium box with holes by Diamond Detector Ldt company. In order to damage both the devices a proton beam was produced by the so called zero degree beam line of the Superconducting Cyclotron at INFN Laboratori Nazionali del Sud Catania (INFN-LNS) with an estimated integrated fluence of $(2.0\pm0.08)\times10^{15}$ protons/cm^2 at an energy of 62 MeV and with a nominal beam current of about 10 nA. The proton bunches were 3 ns long with a period of 25 ns. The irradiation was performed in air and at room temperature

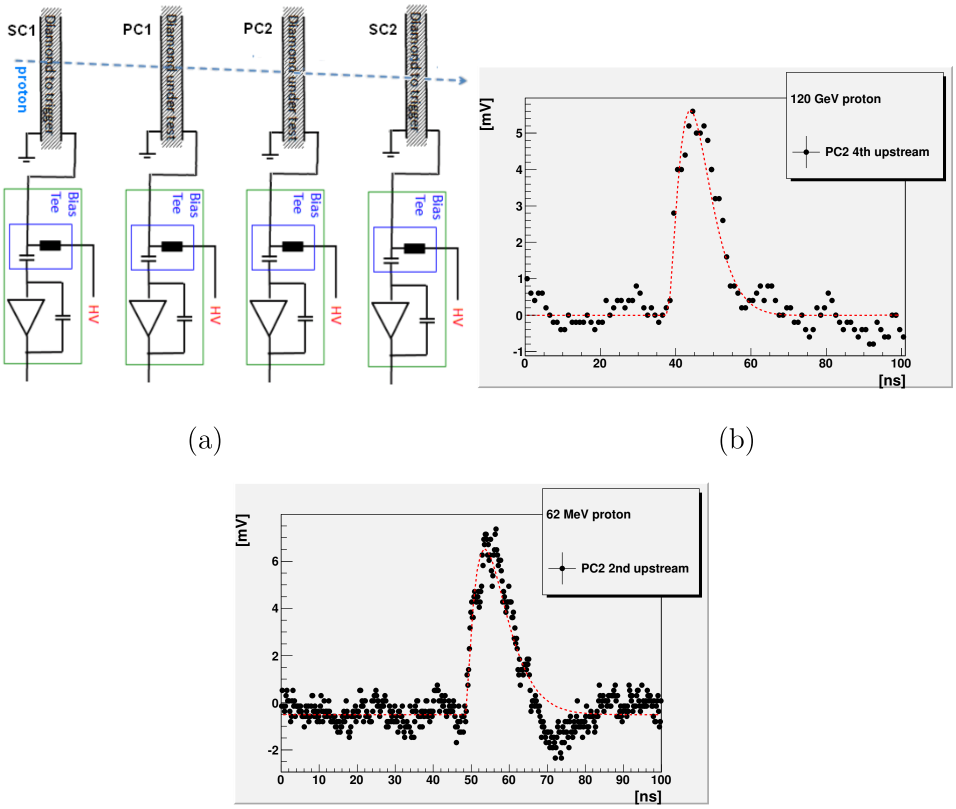

(a) (b)

(c)

Fig. 5.6. (a) Experimental setup used to measure the charge collected by diamond detectors due to the crossing of 120 GeV and 62 MeV proton beams; Typical time profile of the signal induced by a 120 GeV proton (b) and by a 62 MeV proton (c) in polycrystalline diamond detector with laser-graphitized electrodes. The superimposed curve is obtained by the best fit of Eq. 5.5 to the digitized waveform. The data correspond to an applied voltage of +300V.

for 1.5 days during which diamond sensors were biased at 0 V. In Fig. 5.4 (a) we report the picture of the experimental setup employed in the irradiation test.

In order to understand the effects of radiation damage on diamond devices we measured the time responses under β source after and before proton

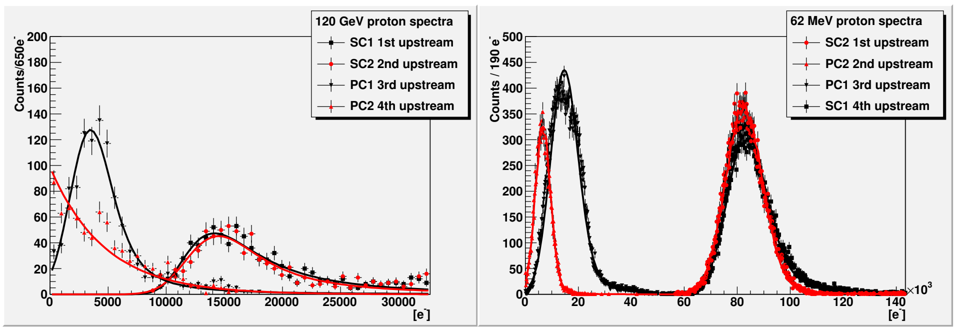

(a) (b)

Fig. 5.7. Charge distribution collected by diamond detectors due to the crossing of 120 GeV protons (a) and 62 MeV protons (b). In this last case the PC1 and PC2 detectors were previously irradiated and damaged. The data correspond to an applied voltage of +300V.

irradiation during which the sensors were polarized at 300 V. We lined up the detectors and exposed them by β electrons as shown in Fig. 5.4 (b) to ensure that a generic β electron across the diamond under test (graphitized diamond) and go toward the diamond to trigger (reference commercial diamond). The signals in output from the devices were collected by two fast charge sensitive amplifiers (gain = 8 mV/fC, time rise = 2 ns, time pulse = 7 ns, noise = 450 e^{-}/pF) and a digital scope. In Fig. 5.5 we report the β time responses before and after protons irradiation. The rise-time of the peaks is dominated by front-end electronics, but no change in pulse shape is observed before and after irradiation for both detectors and consequently no change in time response is evident.

The next step was the extrapolation of λ, the mean free path for electrical carriers in polycrystal diamond bulk, before and after radiation damage in order to have k, the radiation damage constant, to estimate the entity of damage of the detector under test. In order to understand the following passages we define here the charge collection distance $CCD = t\frac{<Q_{col}>}{Q_{gen}}$. For charge collection distance we mean the charge collection efficiency $CCE = \frac{<Q_{col}>}{Q_{gen}}$ normalized to the detector thickness t, where $< Q_{col} >$ is the mean value and not most probably value about collected charge at the output of diamond device and Q_{gen} is the charge generated in diamond bulk by ionizing radiation. The idea is that of measure the CCD for both detectors discussed about previously before and after radiation damage. At this point we call **PC1** the reference commercial diamond and **PC2** our graphitized detector (pad detector). We started with the measure of $< Q_{col} >$ by using the experimental setup in Fig.5.6 (a), but in order to obtain Q_{gen} for our detectors under test, we assume that the CCE of detector grade single crystal diamond is equal to one and in Fig.5.6 (a) we introduced two not irradiated (not damaged) single crystal diamond detectors for the absolute charge calibration (**SC1** and **SC2**). In Fig.5.6 (a) the first amplification stage was the same for the four detectors: a commercial fast charge sensitive amplifier from CIVIDEC having a gain of 8mV/fC and 100 MHz bandwidth with a rise-time and a pulse width of 2 and 7 ns, respectively. The four amplifiers were cross-calibrated by a ramp pulse and each output was normalized by the corresponding calibration constant.

Before irradiation, we had available data from a previous testbeam we did at Fermilab with 120 GeV proton to study timing performance. At Fermilab we used a 1 GHz bandwidth oscilloscope with a digitization frequency of 1Gs/s in order to have CCE before damage.

After irradiation (after damage), we used the same 62 MeV proton beam used for irradiation, but six months later and with a fluence reduced of a 1000 factor respect to the one employed for damage, to measure the charge collection efficiency. At INFN-LNS we used a 4 GHz bandwidth oscilloscope with a digitization frequency of 5Gs/s. No change in output signal shape was notice after irradiation, which is determined by the electronics rise-time and pulse width.

We interpolated the recorded waveforms in Fig.5.6 (b) and (c) with the following formula:

$$V(t) = \begin{cases} V_0 & \text{if } t < t_0 \\ V_0 + V_1 \frac{t-t_0}{t_1} e^{-\frac{t-t_0}{t_1}} P_3(t) & \text{if } t \geq t_0 \end{cases} \tag{5.5}$$

where V_0 is the baseline offset, V_1 is the pulse amplitude, t_0 is the arrival time, t_1 is the rise time, and $P_3(t) = 1 + p_2 t^2 + p_3 t^3$ is a third order polynomial needed to improve the fit of the pulse falling edge. The carrier drift velocity in diamond is about 100 μm/ns. The thickness of the single crystal detectors is about 500μm and than it takes about 5 ns to collect all the charge, which is of the order of the front-end electronics shaping time. We evaluated the collected charge integrating the pulse fit subtracted by the baseline value

$V(t) - V_0$ and the arrival time by the fit constant t_0.

In Fig. 5.7 the charge distributions measured for the four detectors and the two testbeam are reported normalized according to the above prescriptions. The absolute scale is fixed imposing that the average charge of the two single crystal diamond detectors is equal to the expectation. The distributions are fitted with a Landau curve convoluted with a Gaussian curve with the exception of the sensor with graphitized contacts which is fitted with an exponential distribution because it doesn't exhibit a peak in the distribution for the 120 GeV proton. Likely, this is due to the low quality of the sensor bulk and not to the electric contacts because the time response doesn't look problematic and the sensor film was not certified before build the detector.

By the extraction of the mean values for each curve in Fig. 5.7 except for graphitized detector, we measured two CCD values for commercial reference polycrystal diamond (**PC1**) for which one is before and the other is after irradiation damage. In detail if we consider the only charge distribution before irradiation damage we obtain CCD from its definition given above. By making the mean of charge distribution about (**PC1**) device we have $< Q_{col} >$ and in order to have Q_{gen} we calculate the mean value about (**SC1**), because we remember here our assumption that diamond single crystal has a $CCE = 1$. In the same way we measure CCD for (**PC1**) after radiation damage. By using these values of CCD we extrapolate λ and λ_0, i.e. the carrier mean free path after and before irradiation damage, respectively, by employing the following formula [31]:

$$CCD = 2\lambda(1 - \frac{\lambda}{t}(1 - e^{-\frac{t}{\lambda}})), \tag{5.6}$$

which assumes equal mean free path for electrons and holes $\lambda = \lambda_e = \lambda_h$ and extract the radiation damage constant from the formula [31]:

$$\frac{1}{\lambda} = \frac{1}{\lambda_0} + k\Phi \tag{5.7}$$

where Φ is the integrated fluence used to damage the devices. In general k (radiation damage constant) depends on the particle type and energy and we found for 62 MeV protons the value $(1.8 \pm 0.3) \times 10^{-18} \mu\text{m}^{-1}\text{cm}^2$ only for (**PC1**) detector.

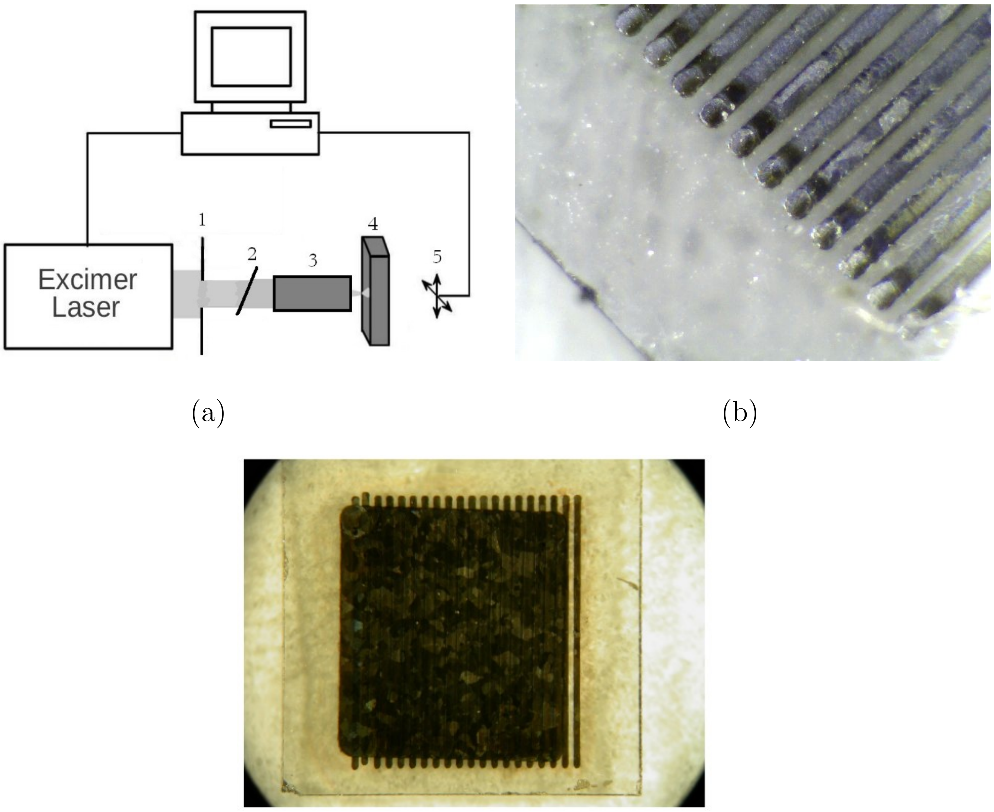

(a)

(b)

(c)

Fig. 5.8. (a) Setup for micro-focusing laser beam. We used an aluminium mask with a square hole (1) and a beamsplitter (2) to divide the laser beam in two parts. One of these parts was directed onto a micro-spot focusing objective (3) to focalize the beam on diamond sample surface (4) that was kept on an automatic moving holder (5); (b) Front view of the detector with graphite micro-strips; (c) Back view of micro-strips device with a uniform graphite electrode of 3 mm × 3 mm.

5.2 Graphitic micro-strips detector

We made a graphitic micro-strips detector based on high quality Chemical Vapor Deposition (CVD) diamond sample. It's the same diamond quality employed for pad detector device described in sections 4.2 and 5.1, but the

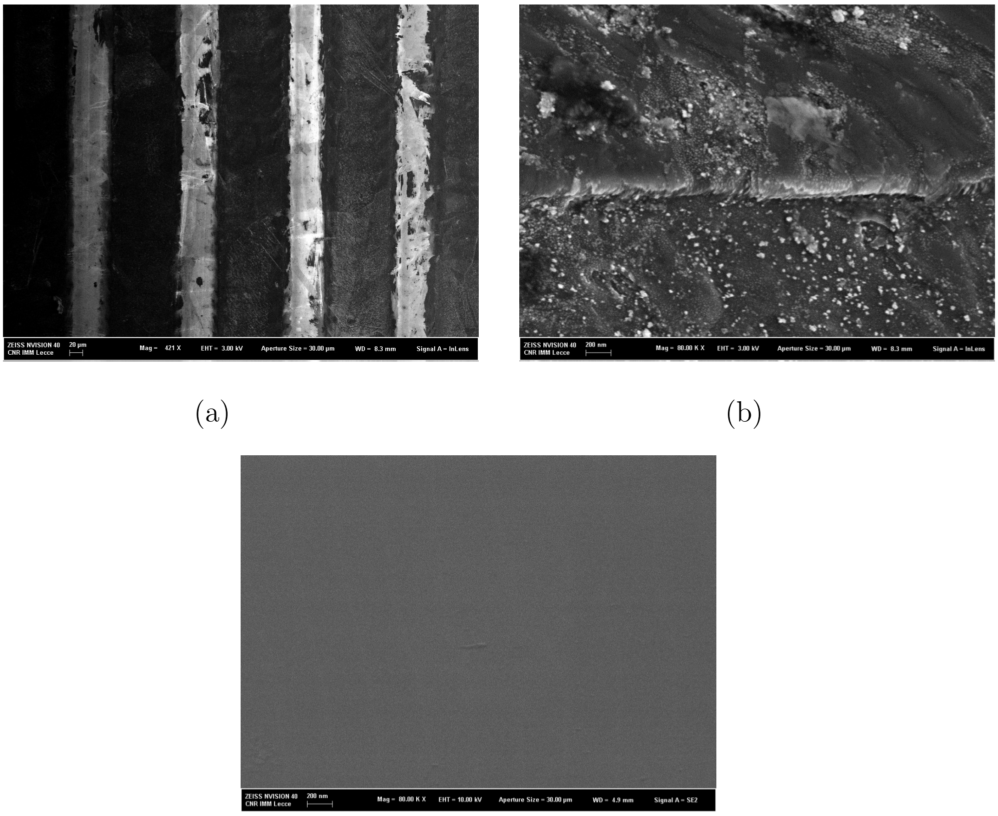

(a) (b)

(c)

Fig. 5.9. SEM micrographs on: (a) micro-strips device (front view), (b) A part of a graphitized strip, (c) unirradiated diamond.

device was made by a different experimental setup [Fig. 5.8 (a)] in order to create 20 graphite micro-strips on front side surface of diamond plate (grow side) [Fig. 5.8 (b)] and on back side (seed side) a uniform graphite pad with a surface of about 3 mm × 3 mm [Fig. 5.8 (c)]. In this case only the 193 nm UV ArF excimer laser (Lambda Physik LPX305i) was employed as in section 4.2. The laser light was directed onto an aluminium mask with a square hole to select only the central part of the beam. The mask was the object and we focused an image on diamond surface by a micro-spot focusing objective,

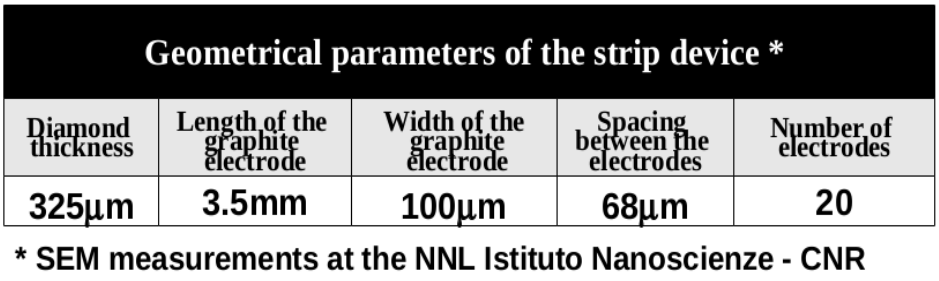

Geometrical parameters of the strip device *				
Diamond thickness	Length of the graphite electrode	Width of the graphite electrode	Spacing between the electrodes	Number of electrodes
325µm	3.5mm	100µm	68µm	20

* SEM measurements at the NNL Istituto Nanoscienze - CNR

Table: 5.2. SEM measurements made on micro-strips device in front side.

15X for 193 nm wavelengths and a numerical aperture (NA) that was 0.32. Before the objective we used a fused silica coated beamsplitter designed for a low transmission ratio of approximately 10-30 % at 193 nm at 45 degrees to reduce the laser power. The beamsplitter divides the laser beam in two parts. One of these parts was directed onto the micro-spot focusing objective to focalize the beam on diamond sample surface and we obtained a circular laser spot with a diameter of about 100 μm and local laser fluence of about 5 J/cm^2. The sample was kept on an automatic moving holder. The holder was a x-y handling stage automatically controlled by a 2D step motors [Fig. 5.8 (a)] that permitted a scanning of the surface at a velocity of about 0.3 mm/s. The device was processed in air and at room temperature. A further analysis was made by collecting SEM images on front view (Fig. 5.9) from which we measured the dimensions of the graphite electrodes (Table 5.2). A preliminary observation shows that graphitized surfaces appear stepped as in section 4.2 for pad detector, with an irregular, dense distribution of nanoparticles partly protruding outwards, but with dimensions that are one order of magnitude smaller than pad detector and vary from 20 nm up to 30 nm. While for unirradiated diamond the surface is uniform [Fig. 5.9 (c)] and this proofs that laser irradiation changes the structure of the sample.

In second analysis an electrical characterization was made on micro-strips device in order to verify the conductivity of the graphitic electrodes and diamond conductivities about the surface and the bulk of the plate by measuring resistivities of these materials. Resistivity of graphitic electrodes was given by transmission line method (TLM) for which in Fig. 5.10 (a) we reported a schematic view of the experimental setup employed. A Yokogawa 7651 programmable DC source was used as a current generator and as a current

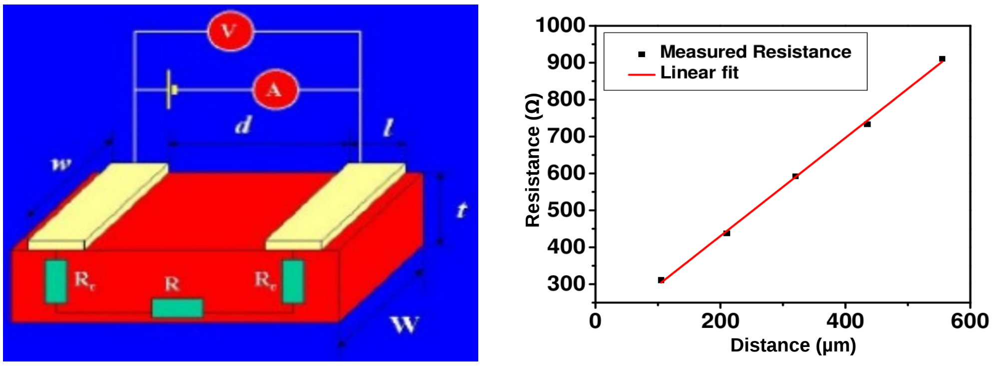

(a) (b)

Fig. 5.10. (a) Schematic of the experimental setup employed to perform TLM measurements on micro-strips diamond device; (b) Resistance measurements made on graphitic micro-strips vs distances as explain in the text.

absorber (sink mode) in order to collect current values in the circuit. While for voltage measurements a digital multimeter HP34401 was employed. For each graphitic strip we placed a couple of probes at different distances each other and for a fixed distance d we measured the Ohmic resistance R_{TOT} between the probes (radius tip 20 μm). In Fig. 5.10 (b) we reported averaged measurements for all graphitic strips, for which a linear fit was made using the following formula:

$$R_{TOT} = 2R_c + \left[\frac{\rho}{wt}\right] d \tag{5.8}$$

where R_c is the contact resistance [Fig. 5.10 (a)], ρ is the graphite resistivity in this case, while w and t are the graphitic strips width and the thickness, respectively. By fixing w at 100 μm (Table 5.2) and t at 60 nm [51] we extrapolated ρ for graphite that is about 3×10^{-6} Ω·m according to tabulated value for natural graphite [61]. By the same method we measured diamond resistivity on the surface applying a variable current between a fixed couple of numbered electrodes (from 11 up to 16) using a Yokogawa 7651 programmable DC source. By the same instrument we collected the current values in the circuit (sink mode), but because of the difficult to detect a signal for the high resistivity of diamond a current amplifier was employed (Femto DLPCA-200 variable gain low noise) and voltage values were given

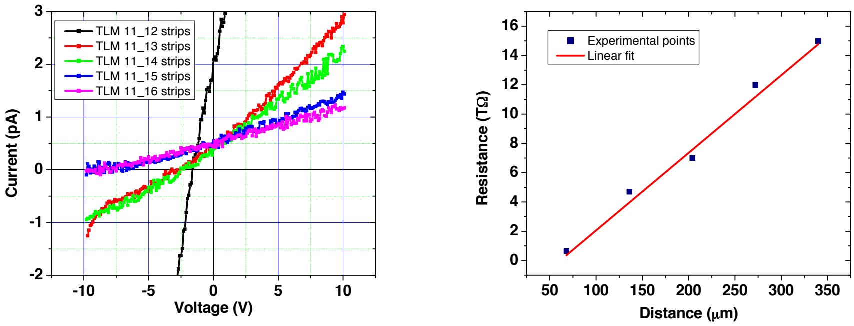

(a) (b)

Fig. 5.11. (a) IV characteristics taken between a fixed couple of numbered electrodes. The fits were performed in the range of voltages from -2 V up to +6 V, where there is a linear response for all measures; (b) Resistance measures obtained from precedent fits vs distances between the fixed couple of numbered electrodes. These measurements were done in dark conditions (without visible light).

by an Agilent 34401A 6 1/2 digital multimeter [Fig. 5.10 (a)]. In details, electrode no. 11 was grounded for all measurements and we polarized the only electrodes from no. 12 up to 16. For each couple of electrodes we measured the IV characteristics in Fig. 5.11 (a) and performed a set of linear fits for each curve in the range of voltages from -2 V up to +6 V, where there is a linear response for all measures. In Fig. 5.11 (b) we reported resistance values obtained from precedent fits vs distances between the fixed couple of numbered electrodes, where red curve is given by Eq. (5.8). By this last plot we extrapolated resistivity for diamond surface that is 6.03×10^{10} $\Omega\cdot$m in dark conditions (without visible light). In order to have a measure for bulk resistivity about diamond plate on the back side of the detector the pad graphite electrode was grounded and we polarized before electrode no.16 and after no.17 and we got the cyclic measurements in Fig. 5.12 from which no hysteresis cycle was seen. We collected leakage current values in presence of visible light and in dark conditions by using the same experimental setup employed to collect IV characteristics between graphite strips (on front side of diamond surface). From plots in Fig. 5.12 two diamond bulk resistivity was given, i.e. in presence of visible light is 4.055×10^{10} $\Omega\cdot$m and in dark

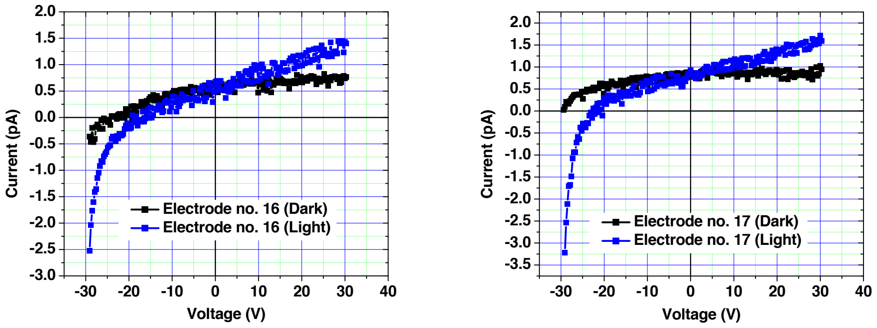

(a) (b)

Fig. 5.12. (a) Diamond bulk leakage current taken between electrode no. 16 and the other electrode on the opposite side (graphite pad). Blue curve was measured in presence of visible light, while black curve in absent of any radiation source; (b) it's the same measure described in (a), but is made with electrode no. 17.

condition is 2.67×10^{11} Ω·m. We realized by this last measures that device can absorb visible light and change the resistivity with a difference of about one order of magnitude. This is an expected results because of polycrystalline nature about our diamond sample. Imperfections in diamonds create electronic and vibronic states in the energy gap, resulting in more than 100 absorption and luminescence centers for diamond spanning from the hard UV to the near infrared [66]. Defects in diamond may be chemical or structural, or a combination of both. Structural defects are lattice imperfections such as dislocations, stacking faults, twin boundaries, and grain boundaries, as well as point defects such as vacancies and divacancies [67]. Another difference we report in this thesis work about the resistivity measurements on the front side between graphite strips that was 6.03×10^{10} Ω·m and the bulk resistivity for leakage current measurements that was 2.67×10^{11} Ω·m. These two values were collected in dark conditions and differ for about one order of magnitude. We realized that diamond surface conductivity is quite different from bulk diamond conductivity for the presence of graphitic states on diamond surface [in refer to Fig. 4.8 (b)].

In order to verify the response in frequency of the micro-strips diamond the device Agilent E4980A Precision LCR Meter was employed to collect

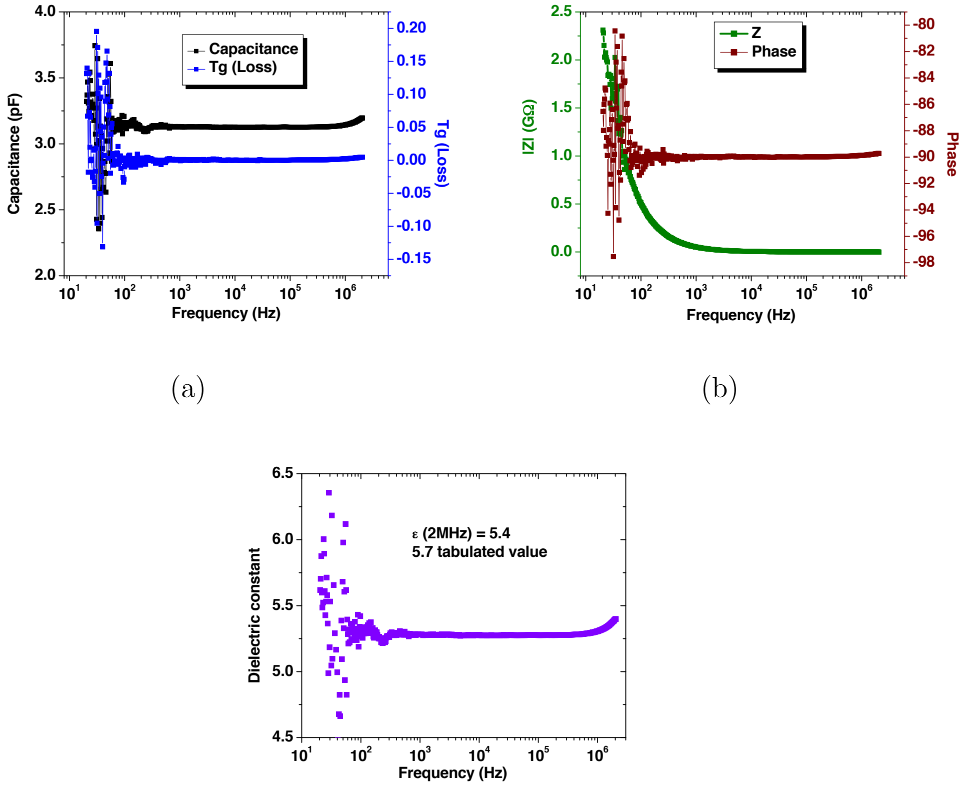

(a) (b)

(c)

Fig. 5.13. (a) and (b) measures of capacitance and impedance vs frequency, respectively, while (c) shows dielectric constant trend vs frequency given by graph (a) modelling diamond device as a planar capacitor.

impedance and capacitance [plots in Fig. 5.13 (a) and (b)]. During these measures diamond sample was blocked between two conductive, planar and metallic electrodes with the purpose to have a parallel plane capacitor with diamond as dielectric medium. By these last plots we extrapolated dielectric constant vs. frequency for diamond plate [Fig. 5.13 (c)] and we found that is 5.4 for a frequency of 2 MHz, while 5.7 is the tabulated value for CVD diamond [68].

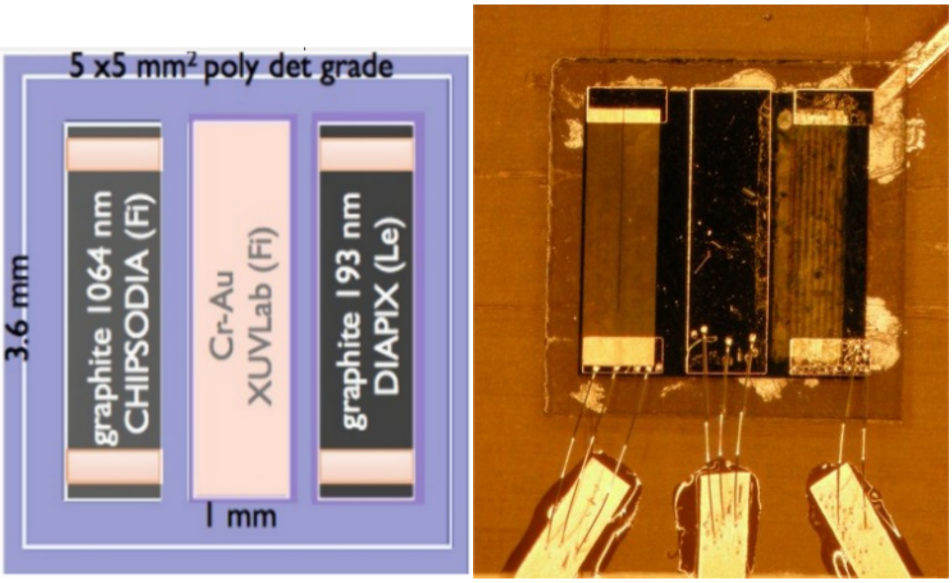

(a) (b)

Fig. 5.14. (a) Schematic view of the three strips detector; (b) Device made according to scheme (a) and glued on a board with contacts (courtesy given by S. Lagomarsino et al. CHIPSODIA Firenze).

5.3 Three strips detector

The aim of the three strips detector is to compare the efficiency of charge collection about three electrodes, made on the same diamond sample. The only difference is that the electrodes made on front surface of diamond were created by different techniques. In Fig. 5.14 (a) the first strip on left side was made by a pulsed ND:YAG laser with duration pulse 8 ns and wavelength 1064 nm. This work was carried out at Firenze (Italy) and is part of a project named CHIPSODIA. They focused laser beam into a spot of 50 μm in diameter and fluence about 5 J/cm^2. They made a scan of diamond surface obtaining a graphite strip with a surface of 1 mm × 3.6 mm. At the center a Cr-Au electrical contact was deposited by thermal evaporation of chromium (50 nm) layer followed by gold (200 nm) layer made in Firenze (Italy) and the name of the project is XUVLab. On the right side of Fig.

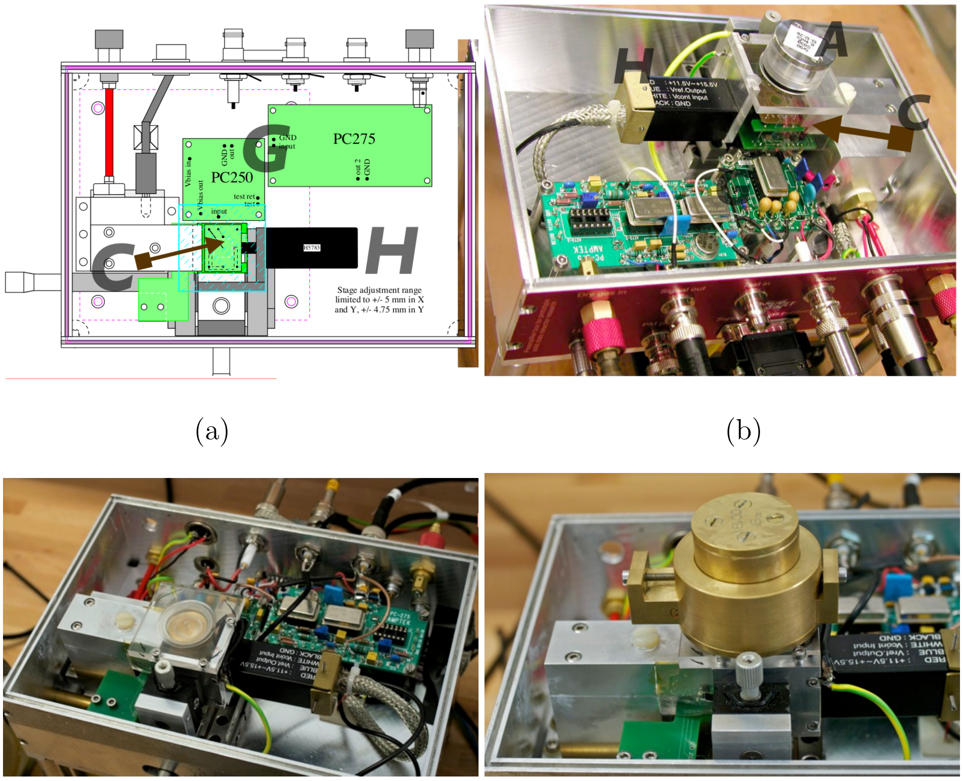

(a) (b)

(c) (d)

Fig. 5.15. Assembly of the sensor holding and its electronic service. (a) Diagram of the electronic used to collect a signal from diamond detector after that β electrons across it; (b) photo of the electronic, where A, C, H, G indicate the most important areas of the system (as explained in the text); (c) perspective view of the station without β source and (d) with β source [area A in Fig. 5.15 (b)] (courtesy given by S. Lagomarsino et al. CHIPSODIA Firenze).

5.14 (a) another graphite strip was create by us at Lecce (Italy) in the project DIAPIX and the layer was made by the same experimental setup described in section 5.2. Fig. 5.14 (b) shows the device made according to scheme (a) and glued on a board with contacts. While on back surface (image not reported) only Cr-Au electrode was deposited with a surface of 3.6 mm × 4

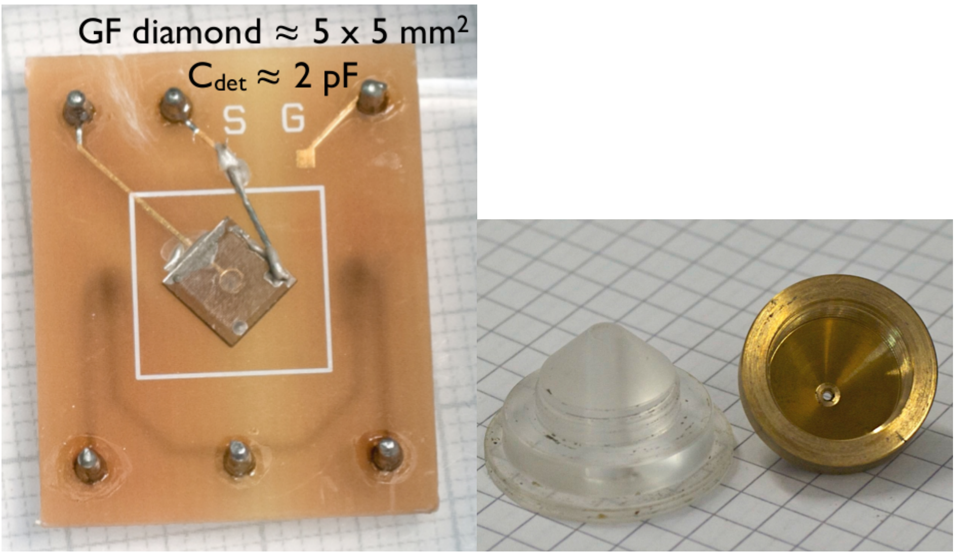

(a) (b)

Fig. 5.16. (a) Printed Circuit Board (PCB) with detector fixed on it; (b) two pieces of the collimator for β electrons (courtesy given by S. Lagomarsino et al. CHIPSODIA Firenze).

mm by the same procedure described for the central strip of Fig. 5.14 (a). A first characterization of the three strips detector was made with a beam of β rays. The β source was ^{90}Sr (^{1}) 0.1 mCi (1994) that emits β with two energies of end point (0.546 MeV and 2.280 MeV). β with energies below 0.75 MeV are easily absorbed by the thickness of the sensor and do not reach the scintillator, all other produce a trigger signal which we interpret as the crossing of a Minimum Ionizing Particles (MIP). Only β electrons with energy greater than 1.5 MeV are MIP and generate 36 pairs e,h/μm in diamond bulk [1]. Taking into account the shape of the energy distribution for the emitted electrons by the source and the cut at 0.75 MeV, the estimate is that only 10% of the trigger signal is due to electrons with energy below 1.5 MeV. At this point in order to measure a particle signal type MIP generated by our new diamond device an experimental setup was prepared. It is a simplified

---

[1] $^{90}_{38}\mathrm{Sr} \ {-}{>}_{(28y)} {}^{90}_{39}\mathrm{Y} {-}{>}_{(64h)} {}^{90}_{40}\mathrm{Zr}$

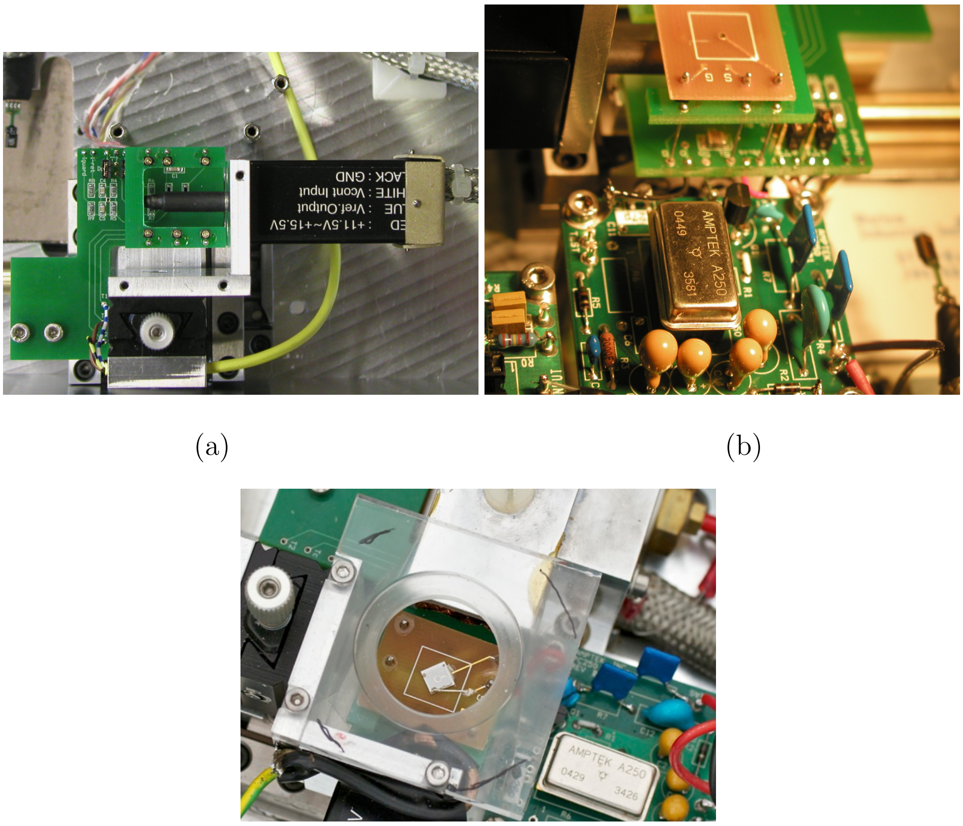

(a)

(b)

(c)

Fig. 5.17. (a) System made by scintillator, guide for the light and photomultiplier; (b) PCB holding mounted over previous system; (c) seen from above about the PCB with the sensor through the support of collimator and the source (courtesy given by S. Lagomarsino et al. CHIPSODIA Firenze).

derivation of the Fred Hartjes's project ([69]). In fact, the automatic controls of the parameters that define the working conditions of the sensor under test such as voltage and temperature are not active. The bias voltage of the sensor (V_B) is manually adjusted (-600 V to 600 V) by the external generator TDK Lambda (19" rack 1 U) connected to the device under test by a HV coaxial cable. Even the power supplies (± 6 V) for electronics and

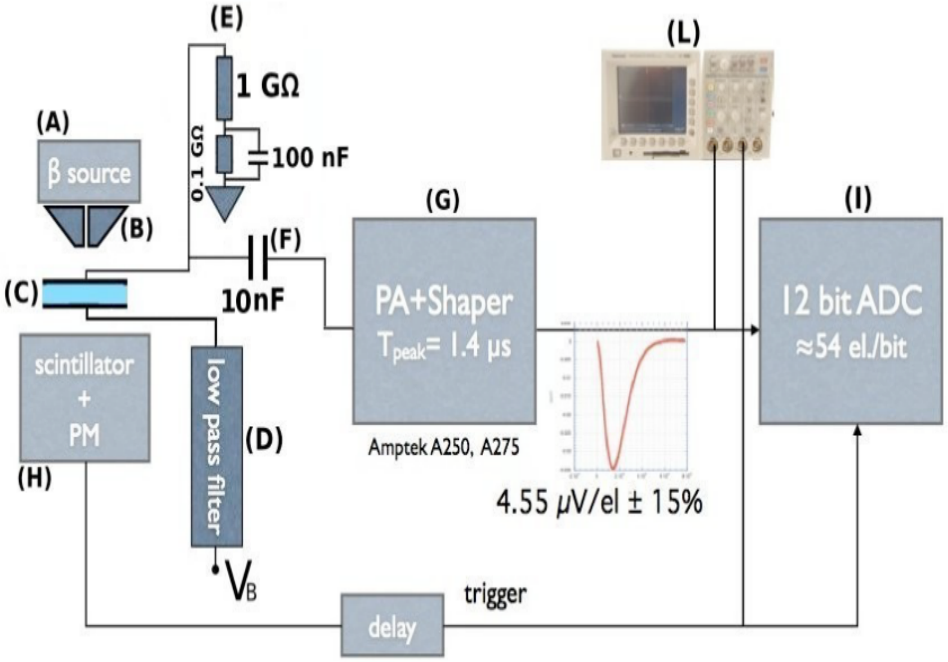

Fig. 5.18. Scheme of the experimental setup employed to measure a signal from three strips detector under β source (courtesy given by S. Lagomarsino et al. CHIPSODIA Firenze).

for the photomultiplier (+12 V, +0.8 V) are activated manually on external generators. Three strips detector, amplifying electronics / training, β source and scintillator for triggering data acquisitions are allocated within a metal box of about 16×23×12 cm^3 (Fig. 5.15) with a brass cover, supported by four small columns. In the box arrive the external power supply and come out two BNC cables in order to have two different signals for output. One is given by three strips detector (signal OUT) after that a β electron go in diamond bulk and the other come from the scintillator placed under diamond device (trigger OUT).

The sensor to be tested is placed on a Printed Circuit Board (PCB) (2.5×2.5 cm^2) has six pins for the external contacts [Fig. 5.16 (a)]. The PCB of the sensor is positioned on a turret [position C of Fig. 5.15 (b)] along which we have the external electrical connections (voltage, input amplifying

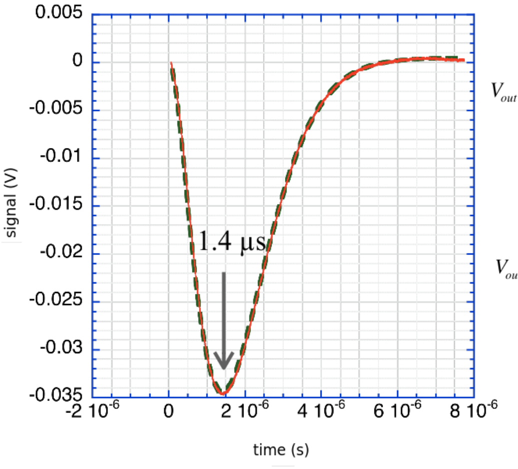

$$V_{out} = \frac{Q_s}{C_f} 34 \left(\frac{t(\mu s)}{0.495} \right)^2 e^{-t(\mu s)/0.79 - t(\mu s)^2 / 4.2^2}$$

$$V_{out\ \max} \approx 41.37 \times \frac{Q_s}{C_f} = 4.55 \frac{\mu V}{electrons} \times Q(electrons)$$

Fig. 5.19. Shape and sensibility of the circuit in Fig. 5.18 (courtesy given by S. Lagomarsino et al. CHIPSODIA Firenze).

electronics and training) [area G of Fig. 5.15 (b)]. Below, in the free part of the turret, we can move a small plastic scintillator (length = 3 mm, diameter = 3 mm) coupled by a light guide of about 2 cm to a photomultiplier (PM) H5783 [2] by using a x-y handling stage manually controlled [area H of Fig. 5.15 (b)]. The scintillator is positioned under the sensor in correspondence with the hole of the PCB. The output signal of the PM is carried out by a BNC connector. A bracket connected with the movement of the scintillator, holds the radioactive source collimator [area A in Fig. 5.15 (b), (c) and (d), Fig. 5.17]. The collimator is a cone of plastic material with a circular hole of 0.6 mm [Fig. 5.16 (b)] on the outer part of which is screwed into the metal hollow cone (brass, tungsten). The source sees the plastic cone while the metal part is directed toward the sensor in order to avoid Bremsstrahlung effects. In Fig. 5.18 is shown the scheme of polarization of the sensor and in Fig. 5.19 the shape and the sensibility of previous circuit. The voltage HV applied on polarized electrodes (strips on diamond front side) of the device is external and the electrode in Cr-Au on back side was kept at ground by

---

[2] The H5783 is a miniature (8 mm diameter) PMT with an adjustable HV generator, in a sealed package (2×2×5 cm^3). Modules require 12 volt power, and a variable voltage, 0 to 1 volt, to adjust the PMT gain. Both voltages are supplied by an external generator.

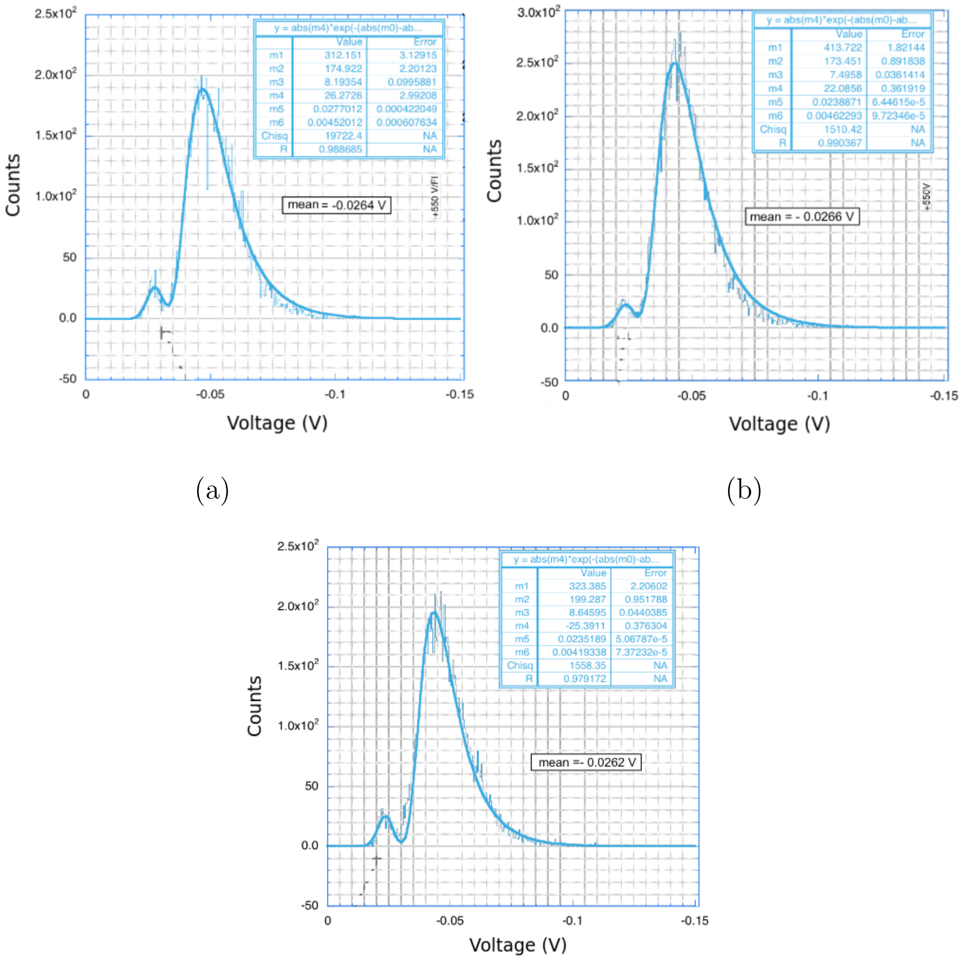

(a)

y = abs(m4)*exp(-(abs(m0)-ab...	Value	Error
m1	312.151	3.12915
m2	174.922	2.20123
m3	8.19354	0.0995881
m4	26.2726	2.99208
m5	0.0277012	0.000422049
m6	0.00452012	0.000607634
Chisq	19722.4	NA
R	0.988685	NA

(b)

y = abs(m4)*exp(-(abs(m0)-ab...	Value	Error
m1	413.722	1.82144
m2	173.451	0.891838
m3	7.4958	0.0361414
m4	22.0856	0.361919
m5	0.0238871	6.44615e-5
m6	0.00462293	9.72346e-5
Chisq	1510.42	NA
R	0.990367	NA

(c)

y = abs(m4)*exp(-(abs(m0)-ab...	Value	Error
m1	323.385	2.20602
m2	199.287	0.951788
m3	8.64595	0.0440385
m4	-25.3911	0.376304
m5	0.0235189	5.06787e-5
m6	0.00419338	7.37232e-5
Chisq	1558.35	NA
R	0.979172	NA

Fig. 5.20. (a), (b) and (c) are three voltage distributions for graphitized electrode by ArF laser, by Nd:YAG laser and deposited Cr/Au contact, respectively. For an applied voltage for each strip of +550 V respect to the other electrode on the opposite side that was kept at ground (courtesy given by S. Lagomarsino et al. CHIPSODIA Firenze).

a resistance of 1 GΩ. This choice is possible for small escape currents from diamond (≤100 fA/cm^2) that make negligible total noise parallel (≈1/R).

The coupling between the sensor and the input of the pre-amplifier is in alternating current (AC) by the capacity of 10 nF, which lets in the very short current pulse (≤1ns) generated by the passage of the particle. The first stage of the pre-amplifier built around the hybrid Amptek A250 with the addition of a FET input (2SK152 n-channel, Sony). The pre-amplifier integrates the charge generated by the sensor on its feedback capacitor ($\approx$ 1 pF). The time constant with which A250 integrates charge is 300 μs for which the feedback resistor is $\approx$ 300 MΩ. The output of the A250 enters in a second PCB equipped with two hybrids A275 (Amptek) whose purpose is to form (filter) the signal of the pre-amplifier in order to maximize the signal/noise ratio. A250 and A275 are in G area at Fig. 5.15 and 5.18. Finally data acquisition is possible by the oscilloscope and by a card ADC 12 bit (National, PCI-6024E). By polarizing the three strips at the same potential (+550V) and keeping at ground the electrode on back side of the detector we obtain the responses (voltage distributions) for each strip in Fig. 5.20. The experimental data was fitted by the following formula [70]:

$$m4e^{-(V-m5)^2/m6^2} + m1e^{-0.5((m2\cdot V-m3)+e^{(-m2\cdot V+m3)})} \tag{5.9}$$

where $m1$ up to $m6$ are fit parameters that we extrapolated and reported in the insets of Fig. 5.20, while the first term in the sum is a Gaussian that we use in order to have an estimate of the noise level and the second term permit to have the mean value of the voltage distributions from which we can conclude that each strip produce the same response under β source.

Conclusions

In this work we irradiated two different types of CVD diamond plate by using an excimer laser working at two different wavelengths: 248 and 193 nm. The first diamond type was a CVD thermal grade and the irradiated areas were characterized by micro-Raman, PL measurements, and SEM images. Using KrF laser, at best, we obtained only disordered graphite, indeed from the micro-Raman D band and G band spectra it is possible to observe a graphite layer when the surface is irradiated with only 10 laser pulses. While, the graphite layer seems to disappear with 200 consecutive laser pulses because the ablation process, which is a competitor of the graphitization process, starts to become predominant. Using ArF laser the micro-Raman measurements point out a spectrum having a single Lorentzian peak at 2720 cm^{-1} with an associated FWHM of about 90 cm^{-1}. The FWHM value means that the surface modified layer is formed by a turbostratic graphite layer. SEM observations confirm our results. Increasing the magnification we observe the distribution of randomly oriented, clearly visible and irregularly shaped flakes, partly protruding outwards from the surface. This is a signature of a t-graphite layer and their average size can be estimated to be about 20-30 nm. By previous results, obtained with ArF, another detector grade diamond sample was graphitized in front and back by the same technique in order to make a diamond device for nuclear applications. Graphite electrodes were characterized with micro-Raman spectra and SEM analysis and we obtained that the layers were graphitic. In addition, by resistance measurements, we demonstrated that the nano-graphitic layers are conductive with an electrical resistivity consistent with the one given in literature for graphite along the perpendicular direction of c-axis [61]. The next step was the measurement of the leakage current along diamond bulk. For this purpose current voltage (IV) characteristics were reported and we saw that for an applied voltages ranging from 0 V to 400 V, we recognized three different conduction regimes: Ohmic-like, Trap Free Space Charge Limited, and Trap Filled Space Charge Limited, without evidence of hysteresis during a cyclic measurement. We analysed the device response to a ^{60}Co γ-rays source and to ultra-relativistic protons, showing that it is capable to work as a radiation detector in counting mode. These preliminary results pave the way to a new method to fabricate metal-less Ohmic contacts on diamond. In order to complete the study, damage measurements were carried out on diamond bulk. A preliminary analysis of radiation damage for polycrystalline diamond was given in terms of time response. We concluded that before and after 62 MeV protons irradiation for a total fluence of $(2.0\pm0.08)\times10^{15}$ protons/cm^2 for 1.5 days, diamond doesn't change in time response if it's tested with a β source. In second analysis we measured polycrystal diamond detectors pulse height before and after 62 MeV proton irradiation using proton beams. The radiation damage was quantified in terms of the relative charge collection efficiency drop using single crystal diamond detector for absolute calibrations. We obtained a radiation damage constant for polycrystal CVD diamond that was k=$(1.8\pm0.3)\times10^{-18}\mu\text{m}^{-1}\text{cm}^2$.

The last work was the fabrication of a new type of device made with graphite micro-strips. We didn't yet characterize this as a nuclear detector, but we demonstrated that it's possible to do micro-writing on diamond surfaces by laser techniques. In this way we made 20 graphite micro-strips on diamond surface with a width of about 100 μm and a spacing between each other of about 68 μm. Electrical and structural measurements on graphite electrodes were carried out in order to confirm the graphitic nature of the layers. Electrical measurements on diamond surface and diamond bulk were performed and we concluded that diamond surface resistivity is one order of magnitude smaller than the one for diamond bulk. This is due to the presence of graphitic state on diamond surface that we saw by micro-Raman analysis made on unirradiated diamond. Capacitance measures vs frequency of diamond bulk gave to us a dielectric constant of 5.4 at 2 MHz, quite consistent with the tabulated value for diamond that is 5.7 [68].

Finally a third device was made with three strips, two graphitic strips in proximity of diamond border and a Chrome-gold (Cr-Au) strip contact at the center. The strips were rectangular with dimensions of 1 mm × 3.6 mm in order to verify the response of the three strips with the same geometry, but made by different technologies. The detector was tested with β radiation at the University of Florence and we measured a voltage distribution for each strip showing a comparable responses respect to each other.

Bibliography

[1] C. Canali, E. Gatti, S. F. Kozlov, P. F. Manfredi, C. Manfredotti, F. Nava, and A. Quirini, "Electrical properties and performances of natural diamond nuclear radiation detectors," *Nucl. Instrum. Methods*, vol. 160, no. 73, 1979.

[2] W. Fallmann, M. Regler, and M. Friedl, "Diamond Detectors for Ionizing Radiation," University of Technology, Vienna, 1999. Electronically available at http://www.hephy.at/user/friedl/da/da.pdf.

[3] G. Davies, *Properties and Growth of Diamond*. London: INSPEC, Institution of Electrical Engineers, 1994.

[4] C. Y. Fong and B. M. Klein, *Electronic and Vibrational Properties of Bulk Diamond*. Boston: Kluwer Academic Publishers, 1995.

[5] K. A. Snail, "Growth, processing and properties of CVD diamond for optical applications," *Opt. Mater.*, vol. 1, no. 4, pp. 235–258, 1992.

[6] S. Coe and R. Sussmann, "Optical, thermal and mechanical properties of CVD diamond," *Diamond and Related Materials*, vol. 9, pp. 1726–1729, 2000.

[7] H. Liu and D. S. Dandy, *Diamond Chemical Vapor Deposition: Nucleation and Early Growth Stages*. New Jersey: Noyes, 1995.

[8] B. V. Derjaguin and D. V. Fedoseev, "The Synthesis of Diamond at Low Pressure," *Scientific American*, vol. 233, no. 5, p. 102, 1975.

[9] B. V. Derjaguin and D. V. Fedoseev, *Growth of Diamond and Graphite From the Gas Phase*. Russian, Moscow: Jzd. Nauka, 1977.

[10] B. V. Spitzyn, L. L. Bouilov, and B. V. Derjaguin, “Vapor growth of diamond on diamond and other surfaces,” *J. of Cryst. Growth*, vol. 52, pp. 219–226, 1981.

[11] M. Kamo, Y. Sato, S. Matsumoto, and N. Setaka, “Diamond synthesis from gas phase in microwave plasma,” *J. Cryst. Growth*, vol. 62, p. 642, 1983.

[12] S. Matsumoto, Y. Sato, M. Tsutsumi, and N. Setaka, “Growth of diamond particles from methane-hydrogen gas,” *J. Mater. Sci.*, vol. 17, no. 11, pp. 3106–3112, 1982.

[13] M. Kamo, H. Yurimoto, and Y. Sato, “Epitaxial growth of diamond on diamond substrate by plasma assisted CVD,” *Appl. Surf. Sci.*, vol. 33/34, pp. 553–560, 1988.

[14] J. Isberg, J. Hammersberg, E. Johansson, T. Wikström, D. J. Twitchen, A. J. Whitehead, S. E. Coe, and G. A. Scarsbrook, “High Carrier Mobility in Single-Crystal Plasma-Deposited Diamond,” *Science*, vol. 297, no. 5587, pp. 1670–1672, 2002.

[15] D. G. Goodwin and J. E. Butler, *Handbook of Industrial Diamonds and Diamond Films*. New York: Marcel Dekker, 1998.

[16] N. Tranchant, M. Nesladek, D. Tromson, Z. Remes, A. Bogdan, and P. Bergonzo, “Time of flight study of high performance CVD diamond detector devices,” *Phys. Status Solidi A*, vol. 204, no. 9, pp. 3023–3029, 2007.

[17] P. W. May, *Diamond thin films*: a 21st-century material, *Phil. Trans. R. Soc. Lond. A*, vol. 358, p. 473-495, 2000.

[18] W. Zhu, B. R. Stoner, B. E. Williams, and J. T. Glass, “Growth and characterization of diamond films on nondiamond substrates for electronic applications,” *Proceedings of the IEEE*, vol. 79, no. 5, pp. 621–646, 1991.

[19] G. Friedbacher, E. Bouveresse, G. Fuchs, M. Grasserbauer, D. Schwarzbach, R. Haubner, and B. Lux, “Pretreatment of silicon substrates for CVD diamond deposition studied by atomic force microscopy,” *Applied Surface Science*, vol. 84, no. 2, pp. 133–143, 1995.

[20] G. S. Ristić, Ž. D. Borgdanov, M. S. Trtica, and Š S. Miljanić, "Diamond deposition on thin cylindrical substrates," *J. Serb. Chem. Soc.*, vol. 76, no. 3, pp. 407–416, 2011.

[21] V. Shanov, R. N. Singh, and W. Tabakoff, "CVD diamond coating for erosion protection at elevated temperatures," *Journal of Materials Engineering and Performance*, vol. 11, no. 2, pp. 220–225, 2002.

[22] P. R. Buerki and S. Leutwyler, "Homogeneous nucleation of diamond powder by CO_2-laser-driven gas-phase reactions," *J. Appl. Phys.*, vol. 69, no. 6, pp. 3739–3744, 1991.

[23] E. K. Spear and M. Frenklach, "High temperature chemistry of CVD (chemical vapor deposition) diamond growth," *Pure & App. Chem.*, vol. 66, no. 9, pp. 1773–1782, 1994.

[24] G. A. Raiche and J. B. Jeffries, "Laser-induced fluorescence detection of polycyclic aromatic hydrocarbons in a dc arcjet used for diamond deposition," *Appl. Phys. Lett.*, vol. 63, no. 22, pp. 3002–3004, 1993.

[25] C. Tang and D. C. Ingram, "The effect of ultrasonic pre-treatment on nucleation density of chemical vapor deposition diamond," *J. Appl. Phys.*, vol. 78, no. 9, pp. 5745–5749, 1995.

[26] M.-R. Shen, H. Wang, Z.-Y. Ning, C. Ye, Z.-Q. Gan, and Z.-X. Ren, "Enhanced diamond nucleation on pretreated silicon substrates," vol. 301, pp. 77–81, June 1997.

[27] S.-S. Park and J.-Y. Lee, "Synthesis of diamond films on titanium substrates by hot-filament chemical vapor deposition," *J. Appl. Phys.*, vol. 69, pp. 2618–2622, 1991.

[28] T. Suzuki and A. Argoitia, "Current Status of Heteroepitaxy of CVD Diamond," *Physica status solidi. A. Applied research*, vol. 154, no. 1, pp. 239–254, 1996.

[29] I. Aharonovich, J. C. Lee, A. P. Magyar, B. B. Buckley, C. G. Yale, D. D. Awschalom, and E. L. Hu, "Homoepitaxial Growth of Single Crystal Diamond Membranes for Quantum Information Processing," *Advanced Optical Materials*, vol. 24, pp. OP54–OP59, 2012.

[30] J. J. Gracio, Q. H. Fan, and J. C. Madaleno, “Diamond growth by chemical vapour deposition,” *J. Phys. D: Appl. Phys.*, vol. 43, pp. 1–22, 2010.

[31] M. Mikuž, “Diamond Sensors,” Presented at ICHEP2012, Melbourne, 6-th July 2012.

[32] E. Berdermann, “Advanced diamond particle detectors,” *Nuclear Physics News*, vol. 19, no. 2, pp. 25–31, 2009. For the NORDIA COLLABORATION.

[33] H. Kagan *et al.*, “Diamond pixel modules,” *Nuclear Instruments and Methods in Physics Research A*, vol. 636, pp. S125–S129, 2011. doi:10.1016/j.nima.2010.04.096.

[34] M. Bruzzi, C. D. Angelis, M. Scaringella, C. Talamonti, D. Viscomi, and M. Bucciolini, “Zero-bias operation of polycrystalline chemically vapour deposited diamond films for Intensity Modulated Radiation Therapy,” *Diamond and Related Materials*, vol. 20, no. 2, pp. 84–92, 2011. DOI: 10.1016/j.diamond.2010.11.011.

[35] S. Almaviva, M. Marinelli, E. Milani, G. Prestopino, A. Tucciarone, C. Verona, G. Verona-Rinati, M. Angelone, D. Lattanzi, M. Pillon, R. M. Montereali, and M. A. Vincenti, “Thermal and fast neutron detection in chemical vapor deposition single–crystal diamond detectors,” *J. Appl. Phys.*, vol. 103, no. 5, p. 054501 (6 pages), 2008. http://dx.doi.org/10.1063/1.2838208.

[36] V. Re, “3D vertical integration technologies for advanced semiconductor radiation sensors and readout electronics,” Advances in Sensors and Interfaces (IWASI), 2011 4th IEEE International Workshop on (pp.33-36). doi: 10.1109/IWASI.2011.6004681. Retrieved from http://hdl.handle.net/10446/25302.

[37] J. Pietraszko, L. Fabbietti, W. Koenig, and M. Weber, “Diamond as timing detectors for minimum–ionizing particles: The HADES proton-beam monitor and START signal detectors for time of flight measurements,” *Nucl. Instr. Meth. A*, vol. 618, pp. 121–123, 2010.

[38] S. Garbolino *et al.*, “Results from the Gigatracker Prototypes: Two Pixel Front-End ASICs with Sub-ns Time Resolution for the NA62 Experiment,” 10th International Conference on Large Scale Applications and Radiation Hardness of Semiconductor Detectors, July 6-8, 2011 (RD11) Firenze (Italy).

[39] S. S. M. Chan, M. D. Whitfield, R. B. Jackman, G. Arthur, F. Goodall, and R. A. Lawes, “The effect of excimer laser etching on thin film diamond,” *Semicond. Sci. Technol.*, vol. 18, pp. S47–S58, 2003.

[40] V. N. Strekalov, V. I. Konov, V. V. Kononenko, and S. M. Pimenov, “Early stages of laser graphitization of diamond,” *Appl. Phys. A*, vol. 76, pp. 603–607, 2003.

[41] V. V. Kononenko, M. S. Komlenok, S. M. Pimenov, and V. I. Konov, “Photoinduced laser etching of a diamond surface,” *Quantum Electronics*, vol. 37, no. 11, pp. 1043–1046, 2007.

[42] V. P. Ageev, L. L. Bouilov, V. I. Konov, A. V. Kuzmichev, S. M. Pimenov, A. A. M. Prokhorov, V. G. R. chenko, B. V. Spitsyn, and B. I. Chapliev *Sov. Phys. Dokl.*, vol. 33, no. 840, 1989.

[43] T. George, M. C. Foote, R. Vasquez, E. P. Fortier, and J. B. Posthill, “Below bandgap laser ablation of diamond for transmission electron microscopy,” *Appl.Phys. Lett.*, vol. 62, no. 22, pp. 2880–2882, 1993.

[44] S. M. Pimenov, A. A. Smolin, V. G. Ralchenko, V. I. Konov, S. V. Likhanski, I. A. Veselovski, G. A. Sokolina, S. V. Bantsekov, and B. V. Spitsyn, “UV laser processing of diamond films: effects of irradiation conditions on the properties of laser-treated diamond film surfaces,” *Diam. Relat. Mater.*, vol. 2, pp. 291–297, 1993.

[45] M. Rothschild, C. Arnone, and D. J. Ehrlich, “Excimer-laser etching of diamond and hard carbon films by direct writing and optical projection,” *J. Vac. Sci. Technol. B*, vol. 4, pp. 310–314, 1986.

[46] C. Johnston, P. R. Chalker, I. M. Buckley-Golder, P. J. Marsden, and S. W. Williams, “Diamond device delineation via excimer laser patterning,” *Diam. Relat. Mater.*, vol. 2, pp. 829–834, 1993.

[47] L. M. Malard, M. A. Pimenta, G. Dresselhaus, and M. S. Dresselhaus, “Raman spectroscopy in graphene,” *Phys.Rep.*, vol. 473, pp. 51–87, 2009.

[48] G. Davies and T. Evans, “Graphitization of Diamond at Zero Pressure and at a High Pressure,” *Proceedings of the Royal Society of London. Series A, Mathematical and Physical Sciences*, vol. 328, pp. 413–427, Jun 1972.

[49] Strekalov and V. N., *Inertial-free amorphization and damage of crystals by laser field*, vol. 3244. Proc. SPIE, 1997.

[50] S. Sciortino, “Growth, characterization and properties of CVD diamond films for applications as radiation detectors,” *RIVISTA DEL NUOVO CIMENTO*, vol. 22, pp. 1–89, April 1998.

[51] J. F. Lin, J. W. Lin, and P. J. Wei, “Thermal analysis for graphitization and ablation depths of diamond films,” *Diamond & Related Materials*, vol. 15, pp. 1–9, 2006.

[52] A. T. Collins, “The Physics of Diamond,” IOS Press,(Oxford, UK, 1997), Edited by A. Paoletti, and A. Tucciarone.

[53] L. Nistor, V. Ralchenko, I. Vlasov, A. Khomich, R. Khmelnitskii, P. Potapov, and J. V. Landauyt, “Formation of amorphous carbon and graphite in CVD diamond upon annealing: A HREM, EELS, Raman and optical study,” *phys. stat. sol. (a)*, vol. 186, no. 2, pp. 207–214, 2001.

[54] K. Iakoubovskii and G. J. Adriaenssens, “Photoluminescence in CVD Diamond Films,” *Physica Status Solidi A*, vol. 172, no. 1, pp. 123–129, 1999.

[55] A. E. Goresy and G. Donnay, “A New Allotropic Form of Carbon from the Ries Crater,” *Science*, vol. 161, no. 3839, pp. 363–364, 1968.

[56] A. Dunlop, G. Jaskierowicz, P. M. Ossi, and S. Della-Negra, “Transformation of graphite into nanodiamond following extreme electronic excitations,” *Phys. Rev. B*, vol. 76, p. 155403, 2007.

[57] T. Oshiro, M. Yamazato, A. Higa, and M. Toguchi, “Raman analysis of trans-polyacetylene chains in hydrogenated amorphous carbon films,” *Japanese Journal of Applied Physics*, vol. 46, no. 2, pp. 756–760, 2007.

[58] A. C. Ferrari and J. Robertson, “Interpretation of Raman spectra of disordered and amorphous carbon,” *Phys.Rev.B*, vol. 61, no. 20, pp. 14095–14107, 2000.

[59] J. R. Hardy and S. D. Smith, “Two-phonon infra-red lattice absorption in diamond,” *Philosophical Magazine*, vol. 6, no. 69, pp. 1163–1172, 1961.

[60] L. J. V. D. Pauw, “A method of measuring specific resistivity and Hall effect of discs of arbitrary shape,” *Philips Research Reports*, vol. 13, pp. 1–9, 1958.

[61] Powell, R.L. & Childs, G.E. (1972), in *American Institute of Physics Handbook*, pp. 4-142 to 4-160.

[62] H. Mathieu , *Physique des semiconducteurs et des composants électroniques*, MASSON (Paris, France, 1996).

[63] J. G. Simmons, “Conduction in thin dielectric films,” *J. Phys. D*, vol. 4, pp. 613–657, 1971.

[64] [Online].Available:
http://www-ppd.fnal.gov/FTBF/.

[65] A. Galbiati, S. Lynn, K. Oliver, F. Schirru, T. Nowak, B. Marczewska, J. A. Dueas, R. Berjillos, I. Martel, and L. Lavergne, “Performance of Monocrystalline Diamond Radiation Detectors Fabricated Using TiW, Cr/Au and a Novel Ohmic DLC/Pt/Au Electrical Contact,” *IEEE Transactions on Nuclear Science*, vol. 56, no. 4, pp. 1863–1874, 2009.

[66] A. T. Collins, “Visible light emission from diamond,” *Proceedings of the Second International Symposium on New Diamond Materials*, in press (1991).

[67] Y. Tzeng, “Diamond Transmissive Windows,” *Diamond Films and Technology*, vol. 1, pp. 31–54, 1991.

[68] [Online].Available:
http://www.cvd-diamond.com/properties_en.htm.

[69] [Online].Available:
http://www.nikhef.nl/I56/.

[70] J. E. Moyal, “Theory of ionization fluctuations,” *Philosophical Magazine Series 7*, vol. 46, no. 374, pp. 263–280, 1955.

Acknowledgments

We acknowledge the support of INFN Technology (Dr. Roberto Perrino) and Interdisciplinary National Scientific Committee (CSN5) through the experiment DIAPIX (DIAmond PIXel); University of Salento for the use of L^3 laser laboratory facility (Dr. A. P. Caricato and Massimo Corrado); Department of Energy, Center for Nano Engineered Materials & Surfaces - NEMAS Politecnico di Milano, Italy for micro- Raman, photoluminescence and SEM measurements; NNL Istituto Nanoscienze - CNR Lecce, Italy for SEM images and electrical measures on the devices (Dr. Giuseppe Maruccio and Dr. Annagrazia Monteduro); University of Firenze, Italy through the experiment CHIPSODIA for β characterizations on three strips device (S. Lagomarsino et al.).